Effect of Ni precursor salts on Ni-mayenite catalysts for steam methane reforming and on Ni-CaO-mayenite materials for sorption enhanced steam methane reforming

A. Di Giuliano, K. Gallucci, P.U. Foscolo, C. Courson

Effect of Ni precursor salts on Ni-mayenite catalysts for steam methane reforming and on Ni-CaO-mayenite materials for sorption enhanced steam methane reforming

A. Di Giuliano[1,2], K. Gallucci[2], P. U. Foscolo[2], C. Courson[1] *

[1] University of Strasbourg, Institut de Chimie et Procédés pour l'Énergie, l'Environnement et la Santé, UMR CNRS 7515, ECPM, 25 rue Becquerel, 67087 Strasbourg cedex 2, FRANCE

[2] University of L'Aquila, Department of Industrial and Information Engineering and Economics, 18 via G. Gronchi, 67100 L'Aquila, ITALY

*Corresponding author: claire.courson@unistra.fr
Université de Strasbourg, Institut de Chimie et Procédés pour l'Énergie, l'Environnement et la Santé, UMR CNRS 7515, ECPM, 25 rue Becquerel, 67087 Strasbourg cedex 2, France
Tel. +33(0)368852770

Abstract

In view of climate change containment, sorption enhanced steam methane reforming (SESMR) appears as an interesting production route for H_2 with the additional advantage of CO_2 capture application performed by high-temperature solid sorbents. CaO is largely employed as CO_2 sorbent because of its low cost mineralized forms (limestone and dolomite), of its high sorption capacity in the high temperature range compatible with steam methane reforming (SMR). Many recent studies have proposed purposely synthesized Ni-based reforming catalysts, used with

high-temperature CO_2 solid sorbents, or combined sorbent-catalyst materials (CSCM). For this last purpose, we studied the effect of Ni salt precursor (Ni nitrate hexahydrate or Ni acetate tetrahydrate) on properties and reactivity of Ni-mayenite catalysts or Ni-CaO-mayenite CSCM, synthesized by an already validated sequence of wet mixing (for

sorbents synthesis) and wet impregnation (for catalysts and CSCM synthesis) methods. Although Ni acetate tetrahydrate was often reported as the best choice to improve textural properties, our study identified Ni nitrate hexahydrate as a definitely more suitable precursor than Ni acetate tetrahydrate in the purpose of developing efficient materials for SESMR. The dissimilar behaviors observed in reforming reactivity are related and explained by the differences in textural properties, Ni species dispersion, and reducibility.

Keywords

Sorption enhanced steam methane reforming

Combined sorbent-catalyst material

Ni salt precursor effect

1 Introduction

Since some decades, H_2 has been considered as a feasible alternative to carbon containing fossil-fuels [1,2], in the framework of growing concerns about anthropogenic greenhouse gas (GHG) emissions and the consequent climate

change [3–8]. Anyway, only in recent years some steps have been made towards the so called “hydrogen economy” (expression introduced by General Motors Co. in 1970 [9]), for instance by studies on fuel cells [10–12], first instalment worldwide of automotve H_2 fuelling stations [13], and the commercialization of first fuel cells electric vehicles [14–16].

At present, Steam Methane Reforming (SMR) of natural gas by Ni-based catalysts, carried out in heated vertical tubular packed-bed reactors (800-1000 °C, 1.5-3.0 MPa), is the most common commercial technology to produce H_2 [4,5,17–21], meeting nearly half of the world demand [9]. In this process, main reactions are actual SMR (Reaction 1) and Water Gas Shift (WGS, Reaction 2) [22–26]:

$$CH_{4(g)} + H_2O_{(v)} \leftrightarrow CO_{(g)} + 3H_{2(g)} \qquad \Delta H^0_{298\,K} = 206.2 \text{ kJ mol}^{-1} \qquad \text{Reaction 1}$$

$$CO_{(g)} + H_2O_{(v)} \leftrightarrow CO_{2(g)} + H_{2(g)} \qquad \Delta H^0_{298\,K} = -41.2 \text{ kJ mol}^{-1} \qquad \text{Reaction 2}$$

Despite its matureness, SMR whole industrial process has some environmental drawbacks, related to GHG emissions and poor energy integration efficiency [27]. Therefore, to establish a virtuous “hydrogen economy”, environmental impact of H_2 production should be contained, as well as its costs, so that SMR and natural gas are still important as a process and a feedstock, respectively [21,28]. Furthermore, United Nations Intergovernmental Panel on Climate Change (IPCC) emphasizes the role of fossil-fuels exploitation together with Carbon Capture and Storage (CCS) as an affordable strategy to limit average global temperature to well below 2 °C above pre-industrial levels [3,29], the target of recent Paris agreement [30].

For these reasons, in recent years researchers have driven their attention towards Sorption Enhanced Steam Methane Reforming (SESMR), a process intensification of SMR (Reaction 1 and Reaction 2) implemented by in-situ CO_2 capture, performed by a high-temperature solid sorbent [21,27,31,32]. CO_2 subtraction from produced gases drags WGS (Reaction 2) equilibrium, and then SMR (Reaction 1), towards further H_2 production, i.e. sorption enhancing [26,33–35]; this allows to obtain a high purity H_2 stream, for instance suitable for applications in solid oxides fuel cells [36,37]. Among high-temperature sorbents, CaO is largely employed since it is easily available in nature in its low-cost mineralized forms (limestone and dolomite), and because of its high sorption capacity (78.6 g_{CO2} per 100 g_{CaO}) and kinetics of its carbonation (Reaction 3) in the high-temperature range [34,38] compatible with SMR.

$$CO_{2(g)} + CaO_{(s)} \leftrightarrow CaCO_{3(s)} \qquad \Delta H^0_{298K} = -178.2 \text{ kJ mol}^{-1} \qquad \text{Reaction 3}$$

SESMR is not already developed at industrial level, as stated in a recent review [39]. Nowadays, experimental studies at laboratory or bench scale have been carried out, mainly focused on searching proper catalysts, sorbents or Combined Sorbent-Catalysts Materials (CSCM) [6,20,40–43]. A common feature among these works is the use of Ni

nitrate hexahydrate as a precursor salt of the catalytic active phase in purposely synthesized materials. As a matter of fact, for transition metals ranging from Mn to Zn, metal nitrates are usually selected as precursors, since they are generally available and cheap, highly soluble in water (more than 4 mol l^{-1}), and decompose at moderate temperatures (below 300 °C) [44].

Nevertheless, literature shows that in several applications different properties and catalytic performances could result because of a change of the Ni salt precursor, all other parameters being equal. Estellé et al. [45] produced NiO by thermal decomposition of Ni nitrate hexahydrate, Ni hydroxide and Ni acetate tetrahydrate: in the first case, highly crystalline NiO with octahedral structures was obtained; in the second, a more amorphous NiO resulted; in the third, together with crystalline NiO, metallic Ni was obtained too, because of CO and H_2 developing during acetate decomposition. Ren et al. [46] demonstrated that Ni/γ-Al_2O_3 catalysts derived from Ni acetate were much more active in the hydrogenation of α-pirene than Ni nitrate derived ones, their Ni fraction being equal; moreover, Ni acetate catalysts were more easily reducible than Ni nitrate ones, thanks to more frequent Ni^{2+} positioning in γ-Al_2O_3 octahedral sites rather than tetrahedral ones. Wu et al. [47] synthesized catalysts with 15 wt% of Ni for glycerol steam reforming, by wet impregnation of commercial γ-Al_2O_3 using Ni nitrate, Ni chloride, Ni acetate and Ni acetylacetonate as precursors: acetate derived catalysts showed the best performances in terms of catalytic activity and H_2 yield, with the lowest quantity of deposited carbon.

In a previous work (Di Giuliano et al. [28]), we followed the most common path, using Ni nitrate hexahydrate to synthesize materials based on mayenite ($Ca_{12}Al_{14}O_{33}$): Ni-mayenite catalysts for SMR, and Ni-CaO-mayenite CSCM for SESMR. Nonetheless and all this considered, in this paper we aim to describe and compare effects linked to the use of Ni nitrate hexahydrate or Ni acetate tetrahydrate as Ni precursors, also combined with the influence of Ni and CaO fraction on properties and reactivity of the same kind of materials for SMR and SESMR.

In order to do so, we adopted the same methodological approach used in [28]; in such a way, results from this previous paper can be properly and fairly used for considerations and comparisons presented in the following. The issue of reactivity resulted very relevant, since investigated materials derived from Ni-acetate were strongly less active in comparison of their homologues synthesized with Ni-nitrate.

2 Materials and methods

2.1 Synthesis method

The synthesis method included a wet mixing procedure to produce solo-mayenite support or CaO-mayenite sorbents, followed by wet impregnation procedure for Ni addition to get Ni-mayenite (SMR catalyst) or Ni-CaO-mayenite

(CSCM for SESMR), respectively. This method is fully described elsewhere (Di Giuliano et al. [28]), and validated for Ni-nitrate as a precursor: it counts several basic steps consisting in mixing in stirred distilled water at 70 °C, room temperature hydration, controlled drying or calcinations, all under air at atmospheric pressure.

Employed precursor salts for mayenite support or CaO-mayenite sorbent preparation were $Ca(CH_3COO)_2 \cdot xH_2O$ (ACROS ORGANICS, purity = 99 %) for calcium, $Al(NO_3)_3 \cdot 9H_2O$ (SIGMA-ALDRICH, purity > 98 %) for aluminium. Nickel precursor salts for wet impregnation were $Ni(NO_3)_2 \cdot 6H_2O$ (SIGMA-ALDRICH, purity > 97 %) or $Ni(CH_3COO)_2 \cdot 4H_2O$ (ALFA AESAR, purity 98 %); from here on, they are shortened by the notations Ni(N) and Ni(Ac), respectively.

2.2 Materials nomenclature

Table 1 lists all materials synthesized in this work, with their nominal composition. Mayenite support or CaO-mayenite sorbent were named as *CaOx*: *x* was the nominal weight percentage of free CaO associated to mayenite (e.g. CaO0 is nominally solo-mayenite, CaO54 is nominally composed by 54 wt% of "free" CaO and 46 wt% of mayenite). SMR catalysts and CSCM were named as *CaOxNi(Y)z*: *CaOx* was fixed according to the starting parent material (CaO0 or CaO54); *Y* specified the precursor salt from which Ni arose, "N" for Ni(N) or "Ac" for Ni(Ac); *z* quantified the nominal weight percentage of metallic Ni varying from 3 to 10 wt%. A study of intermediate Ni contents (4.5 and 6 wt%) confirmed a linear tendency of the catalysts and CSCM properties between these two values.

Table 1: List of synthesized materials.

Name	**Nominal phases**	**Function**	**Nominal free CaO x* [wt%]**	**Nominal Ni z [wt%]**
CaO0	mayenite	inert	0	0
CaO0Ni(N)3	Ni-mayneite	SMR catalyst	0	3
CaO0Ni(N)10	Ni-mayneite	SMR catalyst	0	10
CaO0Ni(Ac)3	Ni-mayneite	SMR catalyst	0	3
CaO0Ni(Ac)10	Ni-mayneite	SMR catalyst	0	10
CaO54	CaO-mayenite	CO_2 sorbent	54	0
CaO54Ni(N)3	Ni-CaO-mayenite	CSCM	52	3
CaO54Ni(N)10	Ni-CaO-mayenite	CSCM	49	10
CaO54Ni(Ac)3	Ni-CaO-mayenite	CSCM	52	3

CaO54Ni(Ac)10	Ni-CaO-mayenite	CSCM	49	10

*for the CSCM named CaO54Ni(Y)z : $Nominal\ free\ CaO\ =\ 54\ \times (1 - z/100)$

2.3 Characterization

Synthesized materials were characterized by: Inductively Coupled Plasma - Atomic Emission Spectroscopy (ICP-AES) for Ca, Al and Ni elemental composition, X-Ray Diffraction (XRD) for crystalline phases identification; Brunauer-Emmett-Teller (BET) and Barrett-Joyner-Halenda (BJH) methods for texture and pores properties; Scanning Electron Microscopy and Transmission Electron Microscopy both combined with Energy Dispersive X-ray Spectrometry (SEM/EDS and TEM/EDS) for morphology and elemental topology; Temperature Programmed Reduction (TPR) for Ni species reducibility.

2.3.1 ICP-AES

Elemental mass percentages of Ca, Al and Ni were detected by a VARIAN 720-ES ICP-AES device. Solid samples were decomposed in a concentrated strong acid, then diluted in deionized water, so to be ready for nebulization operated by the device.

2.3.2 XRD

A BRUCKNER AXS D8 ADVANCED was the device for XRD acquisitions (Bragg angle 2θ = 20 °-70 °, scanning step = 0.0158 °, sampling time = 1 s per step), exploiting CuKα radiation to locate crystalline phases, then identified by Powder Diffraction Files (PDF) of International Centre of Diffraction Data (ICDD) (Table 2).

Table 2: PDF (Powder Diffraction Files) employed for crystalline phase identification in XRD.

Number	**Name**	**Formula**	**Lattice system**	**Bravais lattice**	**2θ for L [°]**
00-009-0413	Mayenite	$Ca_{12}Al_{14}O_{33}$	Cubic	Body-centred	33 ÷ 34
00-037-1497	Lime	CaO	Cubic	Face-centred	32 ÷ 33
00-005-0586	Calcite	$CaCO_3$	Rhombohedral	Primitive	39 ÷ 40
00-044-1481	Portlandite	$Ca(OH)_2$	Hexagonal	Primitive	/
01-070-0134	Calcium aluminium oxide	$CaAl_2O_4$	Monocline	Primitive	/
00-038-1429	Calcium aluminium oxide	$Ca_3Al_2O_6$	Cubic	Primitive	/
00-023-1037	Grossite	$CaAl_4O_7$	Monoclinic	Base-centred	/
00-047-1049	Bunsenite	NiO	Cubic	Face-centred	43 ÷ 44

03-065-2865	Nickel	Ni	Cubic	Face-centred	44 ÷ 45
00-010-0339	Nickel aluminium oxide	$NiAl_2O_4$	Cubic	Face-centred	/

Acquired spectra were also used for the estimation of average crystallite sizes (L) of main detected crystalline phases, by Scherrer equation [48,49] (Equation 1).

$$L = \frac{K\,\lambda}{\beta\cos(2\theta/2)} \qquad \text{Equation 1}$$

Constants K and wavelength of CuKα_1 radiation (λ) were set equal to 0.9 and 0.15406 nm, respectively. Full width at half maximum (β, in radian) and Bragg angle (2θ, in radian) at ray maximum were measured on diffraction rays such that minimum or any overlapping occurred with other ones. For each crystalline phase, the referred ray had the same Bragg angle position in all analysed samples (Table 2).

2.3.3 SEM/EDS

PHILIPS XL30CP was the equipment for SEM (high tension at 20 kV, detector in back scattering electron mode, vacuum in control-pressure mode). Observation were performed on external surfaces of powdery samples and on internal cross-sectional areas of samples embedded in resin and polished with diamond suspensions. In both sample forms, a gold thin layer was deposed by sputtering.

SEM PHILIPS XL30CP carried out EDS analyses by an OXFORD ENERGY 250 INCAx-act LN2-free detector, on spots or zones of external surfaces, or mapping internal cross-sectional areas of embedded samples for elemental topography. Elemental Au could be detected by EDS, even though originally absent in all materials, because of sputtering.

2.3.4 TEM/EDS

TEM micrographs were acquired by a JEOL 2100 (LaB_6 filament) operating at 200 kV, with punctual resolution equal to 0.2 nm in parallel mode and 2-3 nm in Scanning Transmission Electron Microscopy (STEM) mode, equipped with a SDD detector (30 mm^2) for elemental analysis by EDS.

About 10 mg of each powdery sample were firstly ultrasonicated for 5 min in 50 ml of ethanol; 3 or 4 drops of the resulting suspension impregnated the sample-holder (a polymeric membrane sustained by a copper grid). After ethanol evaporation, sonicated particles were then dispersed on the membrane.

2.3.5 Porosimetry

A MICROMERITICS ASAP 2420 analyzer recorded N_2 adsorption and desorption isotherms at -196 °C on previously degassed samples (100-200 mg, 100 µm < d_p < 125 µm). BET specific surface (S_{BET}) and BJH pore specific volume from the desorption isotherm (V_{BJH}) were then calculated.

2.3.6 TPR

Powdery samples (100 mg, 100 µm < d_p < 125 µm), placed in a quartz packed bed reactor, underwent TPR managed by a MICROMERITICS AUTOCHEM II. Each sample was firstly degassed and cleaned from contingent $CaCO_3$ or $Ca(OH)_2$ due to room atmosphere exposure, by a 15 °C min^{-1} heating ramp up to 750 °C, a 30 min step at 750 °C and a cooling down to room temperature, all under a 50 Nml min^{-1} Ar stream. Actual TPR followed, including a 15 °C min^{-1} heating up to 1000 °C and a 30 min step at this temperature, under a reducing flowrate of 50 Nml min^{-1} (10 vol% of H_2 in Ar). Afterwards, the sample was cooled to room temperature under Ar flow.

2.4 Reactivity tests

The packed bed microreactor rig utilized in this work, was fully described in [28], as well as related experimental procedures for SMR tests on Ni-mayenite catalysts and SESMR tests on Ni-CaO-mayenite CSCM. Anyway, in the following subsections main information is summarized for the sake of clarity. Typical operating conditions [6,39,40,50-56] were chosen for SESMR experiments on the investigated kind of materials.

2.4.1 Packed bed microreactor apparatus

The particulate solid sample (500 mg, 100 µm < d_p < 125 µm) was placed in a vertical packed bed quartz reactor heated by cylindrical electric furnace, fed with H_2, CH_4, N_2 as internal standard, Ar as diluent, and steam obtained from vaporization of demineralized water. Downstream the reactor, an ice trap condensed residual water while other gases went towards two Gas Chromatographs in series equipped with Thermal Conductibility Detectors (GC/TCD), which identified H_2, N_2, CH_4, CO and CO_2 and quantified their concentration ($cGC_{i,out}$). Assuming N_2 flowrate ($F_{N2,in}$) to be constant throughout the whole process, products flowrates ($F_{i,out}$) were consequentially calculated (Equation 2).

$$F_{i,out} = \frac{cGC_{i,out}}{cGC_{N_2,out}} \cdot F_{N_2,in} \quad ; \quad i = CH_4, H_2, CO, CO_2 \qquad \text{Equation 2}$$

2.4.2 SMR tests on Ni-mayenite catalysts

The first step was the pre-reduction (10 °C min^{-1} heating ramp until 900 °C, then 1 h at 900 °C under a reducing flow with 20 vol% of H_2 balanced by inert gases), so to get metallic Ni, which is the reforming catalytic active phase. After

that, the reactor was cooled under an Ar stream, until the temperature of reforming. Two different procedures were applied:

- SMR-1: after Ar cooling, temperature was kept at 850 °C for 1 h, then at 750 °C for 1 h and in the end at 650 °C for 1 h, feeding 2 Nml min^{-1} of CH_4, 2 Nml min^{-1} of N_2, 10 Nml min^{-1} of Ar and steam (molar inlet steam/carbon ratio equal to 3).
- SMR-2: after SMR-1 procedure, reactor was cooled down to room temperature and then heated up to 650 °C under Ar; at 650 °C SMR was newly started with the same inlet of SMR-1, lasting for 3 h.

The first procedure (SMR-1) evaluated the catalyst efficiency under usual SMR conditions (temperature higher than 800°C) and followed its behavior at lower temperatures (until 650°C) allowing both CO_2 sorption and methane reforming. The second procedure (SMR-2) permitted to check the upkeep of the catalyst efficiency at 650°C.

2.4.3 SESMR tests on Ni-CaO-mayenite CSCM

Pre-reduction step described in §2.4.2 was applied for CSCM too, then the reactor was cooled down to 650 °C under an inert Ar stream, and at this temperature reforming started by switching the feeding stream from Ar to the same inlet flows adopted for SMR test (§2.4.2).

2.4.4 Data elaboration

Weight Hourly Space Velocity (WHSV, Equation 3) and Nickel Weight Hourly Space Velocity (Ni-WHSV, Equation 4) identified test conditions, while reactivity performances were evaluated in terms of CH_4 conversion (χ_{CH4}, Equation 5) and product concentrations on dry and diluent-free basis ($C_{i,out}$, Equation 6). The choice of inlet flowrates and packed mass resulted from the compromise between the purpose to obtain high enough WHSV and Ni-WHSV (at least comparable with literature [6,39,40,50-56]) and the need to have a sufficiently long sorption enhancing period to be detected with GCs (one sampling each 5 min). When nominal Ni weight fraction (w_{Ni}) is considered, Equation 4 provides "Nominal Ni-WHSV"; whereas when w_{Ni} is that measured by ICP-AES (§3.1.1), Equation 4 provides the "Actual Ni-WHSV".

$$WHSV = \frac{F_{CH4,in}}{m} \qquad \text{Equation 3}$$

$$Ni\text{-}WHSV = \frac{F_{CH4,in}}{m \cdot \left({}^{w_{Ni}}/_{100}\right)} \qquad \text{Equation 4}$$

$$\chi_{CH_4} = \frac{F_{CH4,in} - F_{CH4,out}}{F_{CH4,in}} \cdot 100 \qquad \text{Equation 5}$$

$$C_{i,out} = \frac{F_{i,out}}{\sum_j F_{j,out}} \cdot 100 \quad ; \quad i,j = CH_4, H_2, CO, CO_2$$ Equation 6

3 Results and discussion

3.1 Characterization of as-synthesized CSCM

3.1.1 ICP-AES

A first evidence about syntheses came from elemental Ca, Al and Ni quantification by ICP-AES, compared for each material with corresponding nominal fractions in Table 3. Since ICP-AES was performed on as-synthesized materials, nominal compositions were calculated for this state, i.e. assuming nominal Ni to be in the form of NiO. Indeed, last step of wet impregnation is a calcination [28]. Most of the experimental ICP-AES values agree with nominal compositions. No clear relation emerges between slight discrepancies detected and parameters investigated (Ni precursor, free CaO fraction, Ni fraction), therefore they could be ascribed to experimental variability in individual syntheses.

Table 3: Nominal elemental contents and ICP-AES experimental results for as-synthesized materials.

	Nominal content				**ICP-AES results**			
Material	**Al [wt%]**	**Ca [wt%]**	**Ni [wt%]**	**Ca/Al [wt/wt]**	**Al [wt%]**	**Ca [wt%]**	**Ni [wt%]**	**Ca/Al [wt/wt]**
CaO0	27.2	34.7	0	1.3	28.1	36.0	-	1.3
CaO0Ni(N)3	26.2	33.4	3.0	1.3	28.7	37.3	2.9	1.3
CaO0Ni(N)10	23.9	30.4	9.7	1.3	24.3	31.7	11.7	1.3
CaO0Ni(Ac)3	26.2	33.4	3.0	1.3	27.9	37.0	3.1	1.3
CaO0Ni(Ac)10	23.9	30.4	9.7	1.3	25.8	33.9	10.1	1.3
CaO54	12.5	54.5	0.0	4.4	12.6	55.0	-	4.4
CaO54Ni(N)3	12.1	52.5	3.0	4.4	10.3	47.0	2.4	4.6
CaO54Ni(N)10	11.0	47.8	9.7	4.4	11.0	48.0	9.3	4.4
CaO54Ni(Ac)3	12.1	52.5	3.0	4.4	10.1	47.0	2.5	4.7
CaO54Ni(Ac)10	11.0	47.8	9.7	4.4	11.5	48.0	9.8	4.2

3.1.2 Crystalline phases

X-ray diffractograms in Figure 1 and Figure 2 show crystalline phases detected in as-synthesized materials: in all cases, desired phases appeared ($Ca_{12}Al_{14}O_{33}$, CaO, NiO) and rays intensities were qualitatively in agreement with expected nominal compositions.

CaO0 sample (mayenite) which was expected to contain uniquely $Ca_{12}Al_{14}O_{33}$, also contained $CaAl_2O_4$ traces and CaO (Figure 1), the presence of which was explained by hypothesizing a partial tendency of Ca species to be not involved in reactions with Al ones; contingent $CaAl_2O_4$ formation was found to be resolved only by a high free CaO excess [28]. Consequently, Ni-mayenite SMR catalysts (Figure 1) has some $CaAl_2O_4$, while CSCM descending from CaO54 are $CaAl_2O_4$-free, at least as a result of XRD analyses (Figure 2).

XRD spectra of Ni-mayenite SMR catalysts (Figure 1) and CSCM (Figure 2) proved that the wet impregnation procedure was effective in the addition of Ni, whatever the Ni salt precursor (nitrate or acetate). It appeared in the form of NiO, as the last step in the procedure is a calcination: the higher Ni nominal fraction, the more intense NiO main ray (Bragg angle at about 43 °, Figure 1 and Figure 2).

Generally, $Ca(OH)_2$ and $CaCO_3$ phases could be ascribed to the exposure to ambient conditions (Figure 1 and Figure 2).

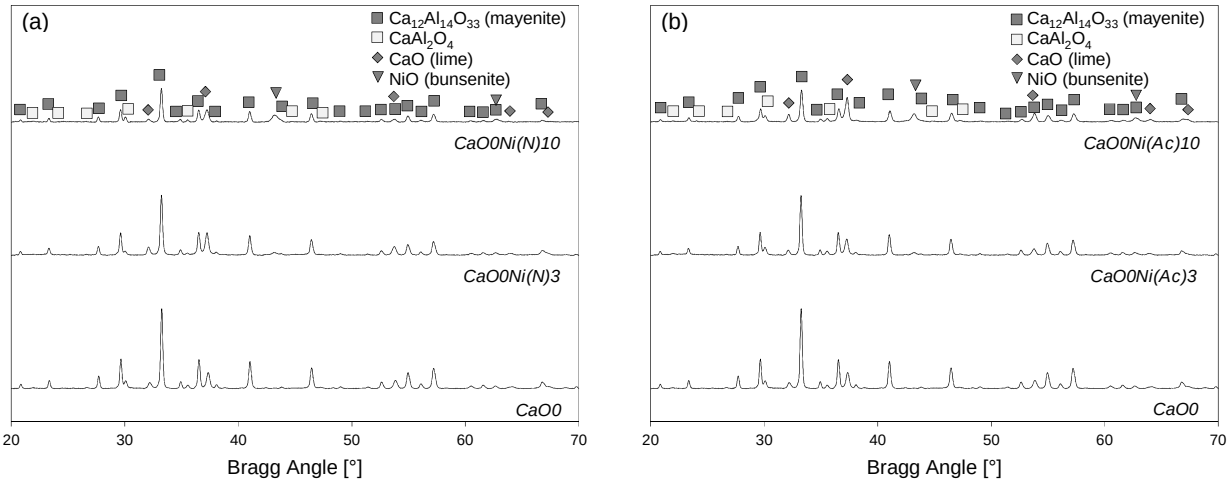

Figure 1: X-ray diffractograms of Ni-mayenite SMR catalyst, impregnated with (a) Ni(N) and (b) Ni(Ac), compared with CaO0.

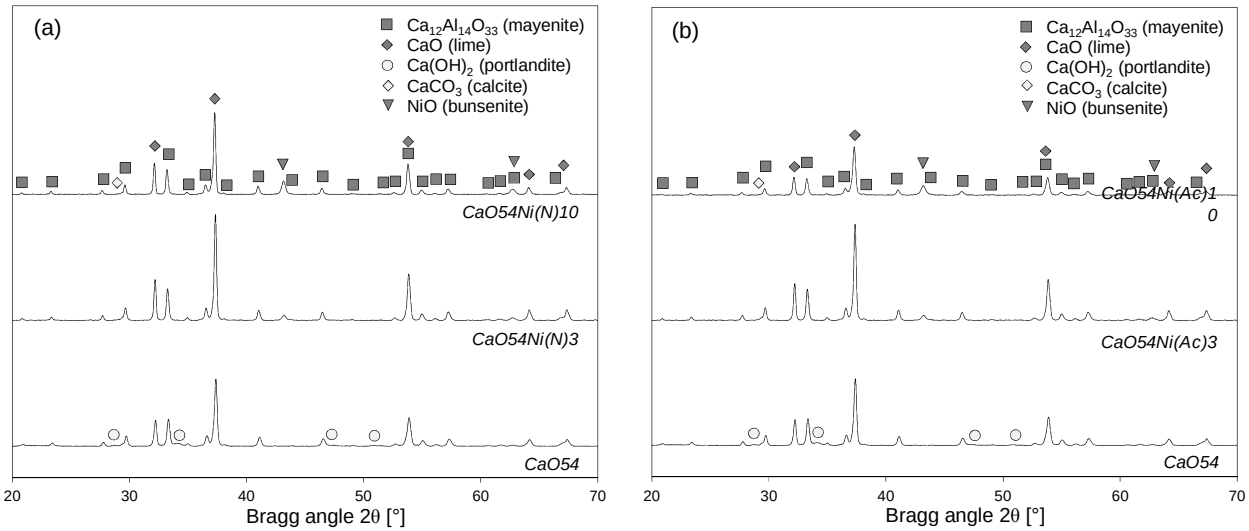

Figure 2: X-ray diffractograms of CaO54Ni(Y)z impregnated with (a) Ni(N) and (b) Ni(Ac) compared with CaO54.

Tables 4 and 5 report average crystallite sizes estimated by Scherrer equation (Equation 1). For each considered phase, dimensions are quite uniform. A tendency of CaO (Table 4) and NiO (Table 5) crystallite sizes to enlarge could be observed with increasing CaO fraction (i.e. decreasing mayenite fraction), confirming mayenite dispersion effect, documented as a strategy to limit CaO sintering, which causes CaO sorption capacity decay in multicycle sorption/calcination usage [34].

Table 4: Average crystallite size (L) estimation by Scherrer equation for the main Ca phases detected by XRD in as-synthesized materials (As-synth.), after TPR (TPR) and after SMR and SESMR tests (Test).

Material	**$Ca_{12}Al_{14}O_{33}$ [nm]**			**CaO [nm]**			**$CaCO_3$ [nm]**
	As-synth.	**TPR**	**Test**	**As-synth.**	**TPR**	**Test**	**Test**
CaO0	37.0	/	/	23.8	/	/	/
CaO0Ni(N)3	35.0	37.4	36.7	28.4	34.2	/	29.8
CaO0Ni(N)10	32.9	40.1	38.4	26.6	32.8	/	31.6
CaO0Ni(Ac)3	35.1	39.5	38.8	27.5	34.0	35.0	/
CaO0Ni(Ac)10	32.3	37.9	38.2	31.8	33.3	34.4	/
CaO54	31.4	/	/	36.4	/	/	/
CaO54Ni(N)3	34.4	37.7	35.5	38.3	40.7	38.1	33.4
CaO54Ni(N)10	36.2	32.9	35.8	40.7	30.9	40.3	28.4
CaO54Ni(Ac)3	33.2	36.2	35.6	37.4	40.3	38.8	/
CaO54Ni(Ac)10	30.8	33.9	36.4	34.6	39.0	39.6	/

Table 5: Average crystallite size (L) estimation by Scherrer equation for the main Ni phases detected by XRD in as-synthesized materials (As-syn), after TPR (TPR) and after reforming tests (Test).

Material	NiO [nm]	Ni [nm]	
	As-synh.	TPR	Test
CaO0	/	/	/
CaO0Ni(N)3	15.9	29.0	27.3
CaO0Ni(N)10	13.8	29.6	28.5
CaO0Ni(Ac)3	17.9	25.8	24.9
CaO0Ni(Ac)10	17.4	25.9	25.5
CaO54	/	/	/
CaO54Ni(N)3	21.1	28.5	25.9
CaO54Ni(N)10	22.1	27.6	27.6
CaO54Ni(Ac)3	21.1	31.1	36.7
CaO54Ni(Ac)10	18.8	31.2	29.7

All these observations brought to the conclusion that no appreciable difference came from Ni(N) or Ni(Ac), as far as formation of crystalline phases is concerned. However, a higher NiO crystallite size is noticeable for CaO0Ni(Ac)z compared to CaO0Ni(N)z, particularly for z = 10 despite a slight lower Ni content measured in CaO0Ni(N)10 (Table 3).

3.1.3 SEM/EDS

SEM micrographs of as-synthesized samples generally highlighted a common microgranular external structure, with porosity in the form of irregular holes and slits, with the unique exception of CaO0, having cubic formations (Figure 3). EDS on external surfaces of CaO-sorbents and CSCM (not shown) detected elemental Ca and Al with different semi-quantitative molar ratios in different spots or zones, in accordance with desired presence of “free” CaO on mayenite, proved by XRD (§3.1.2); moreover, Ni was found in Ni-mayenite catalysts and CSCM.

none

CaO0

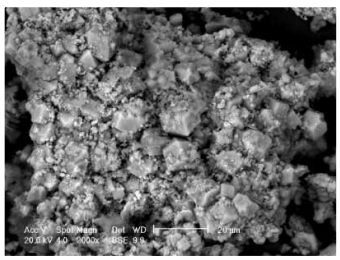

CaO54

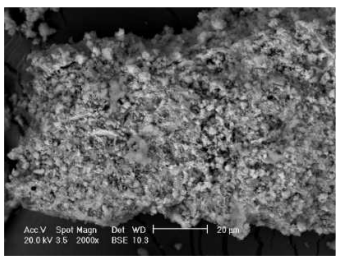

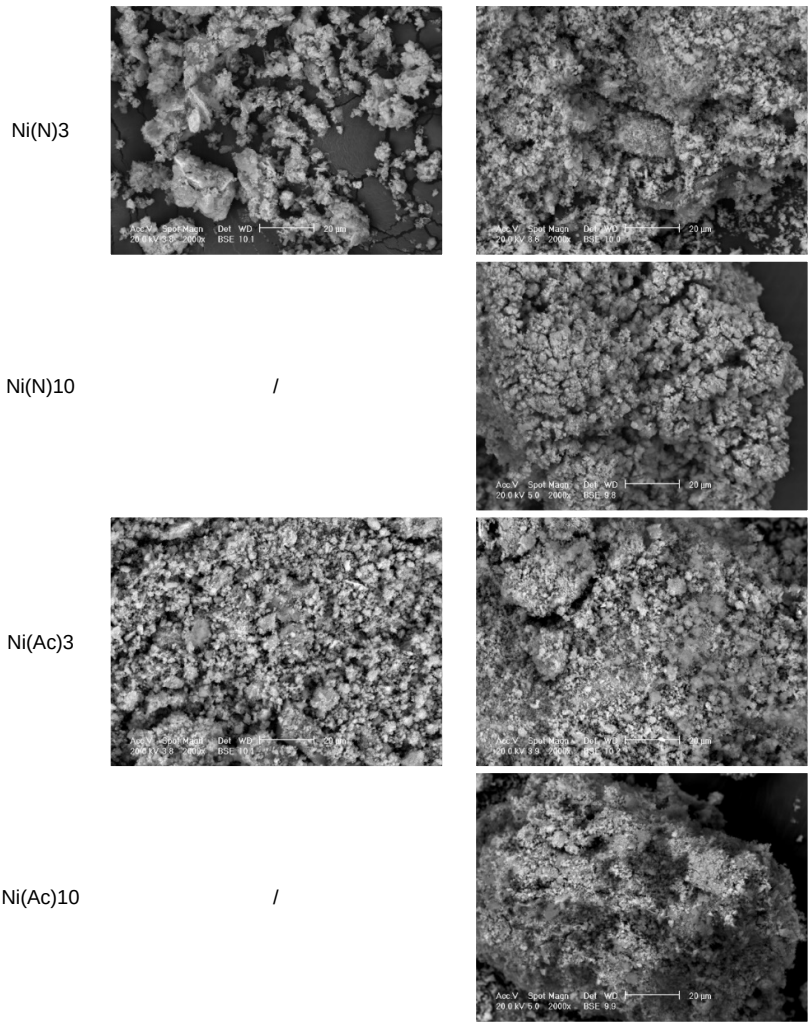

Figure 3: SEM micrographs at 2000x magnification of as-synthesized materials: columns divided by parent material ("free" CaO content), rows by nominal nickel content and precursor salt.

EDS on cross sectional areas of embedded CSCM (Figure 4) located elemental Ni mainly in external shells enveloping particles, or in veins adherent to their internal voids, without significant distinctions between Ni(N) and Ni(Ac) deriving products.

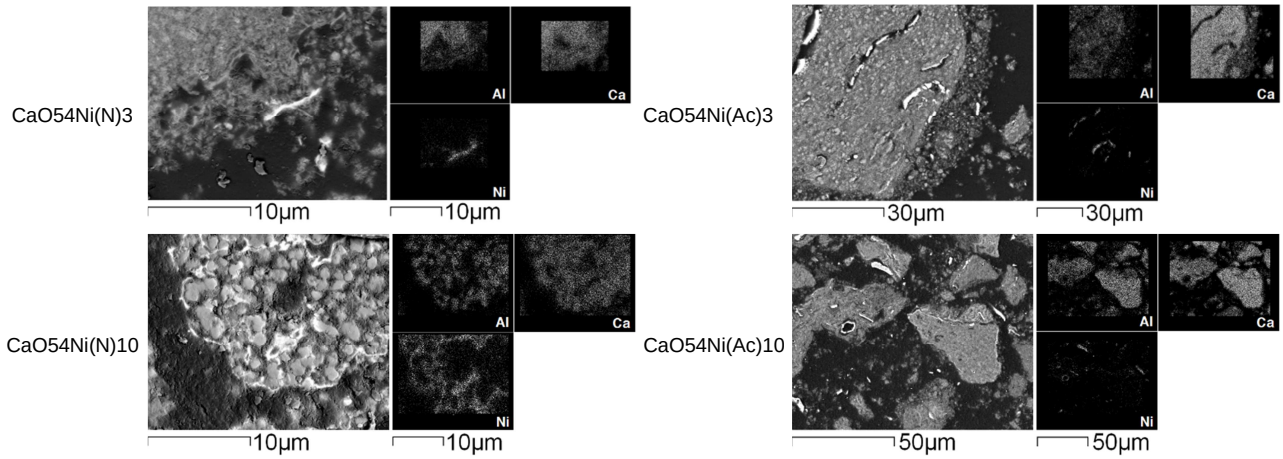

Figure 4: SEM-EDS map for embedded CaO54Ni(Y)z CSCM in as-synthesized state; columns divided by precursor salt (Y), rows by nominal nickel content (z).

3.1.4 TEM/EDS

TEM micrographs of Ni-mayenite SMR catalysts with 10 wt% of Ni (Figure 5) permitted to observe dark spheroidal particles of NiO, dispersed on a mayenite matrix, as confirmed by cross-correlating XRD spectra (Figure 1) and STEM-EDS elemental analysis, detecting Ni preponderance in spheroids and Ca/Al ratio close to that of $Ca_{12}Al_{14}O_{33}$ in the surrounding matrix. These micrographs also evidence a better NiO dispersion on mayenite matrix in CaO0Ni(N)10 than in CaO0Ni(Ac)10.

Magnifications at 20 nm (Figure 5) showed that NiO spheroids dimensions were comparable to *L* estimates (Table 4), and evidenced a difference between Ni(N) and Ni(Ac) derivation, as NiO particles in CaO0Ni(N)10 were surrounded by a shell, while they were not in CaO0Ni(Ac)10. An additional feature encountered only in CaO0Ni(Ac)10 was the detection of whirl-like structures (Figure 6), compatible with carbon black formations [57] and therefore most likely ascribable to the decomposition of acetate species in nickel carbide due to substoichimetric O_2 atmosphere in the inner bulk of material, as previously observed [58].

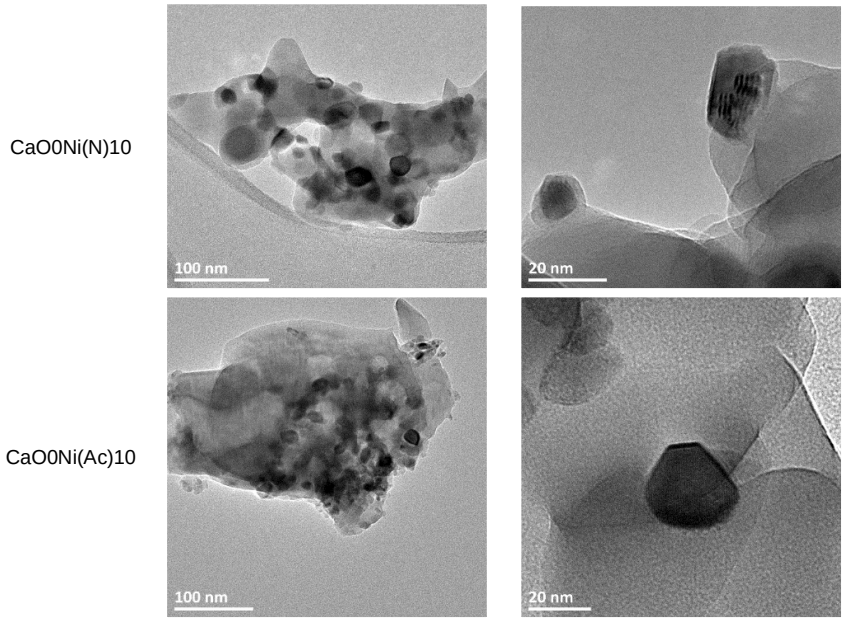

Figure 5: TEM micrographs of as-synthesized CaO0Ni(N)10 (first row) and CaO0Ni(Ac)10 (second row).

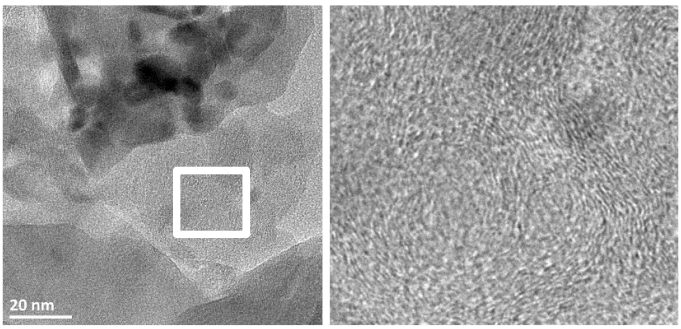

Figure 6: TEM micrograph of as-synthesized CaO0Ni(Ac)10 (on the left) with graphical magnification of the zone within the white box (on the right).

3.1.5 Porosimetry

As far as Ni-mayenite SMR catalysts are concerned, nominal Ni fraction and its precursor salt affected pores properties (Figure 7). In the case of Ni(N) catalysts, S_{BET} was always increased with respect to CaO0, with a slight negative trend as the nominal Ni fraction increased (Figure 7a); V_{BJH} of CaO0Ni(N)3, as well as V_{BJH} of CaO0Ni(N)4.5 and of CaO0Ni(N)6 (not shown), is higher than that of CaO0, however the contrary happens for CaO0Ni(N)10, revealing a negative influence of Ni fraction increase (Figure 7b). For Ni(Ac) catalysts, a similar trend could be inferred, however quantitatively more evident; in fact, S_{BET} and V_{BJH} decreased more markedly as nominal Ni fraction increased, with values significantly lower than that of CaO0 for 10 wt% of Ni (Figure 7) and 6 wt% (not shown). The nominal Ni fraction being equal, Ni-mayenite samples impregnated with Ni(N) always showed higher S_{BET} and V_{BJH} than corresponding ones impregnated with Ni(Ac). These comparisons were performed at the same Ca/Al ratio (Table 3).

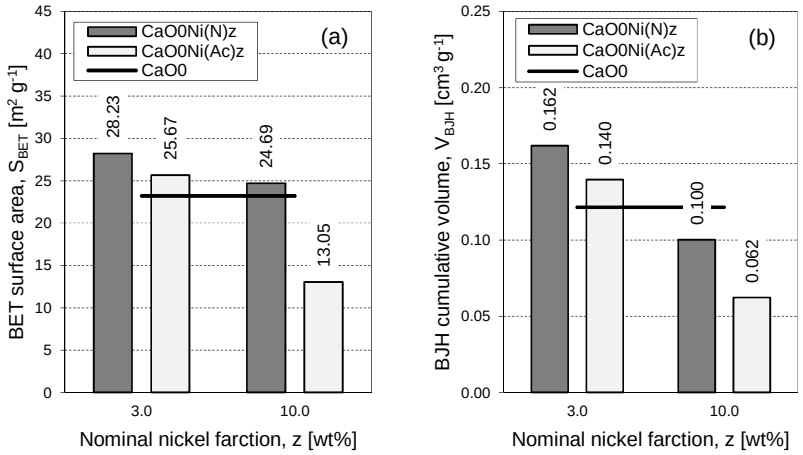

Figure 7: (a) BET surface areas (S_{BET}) and (b) BJH cumulative volumes (V_{BJH}) for Ni-mayenite SMR catalysts, with corresponding CaO0 values as a reference.

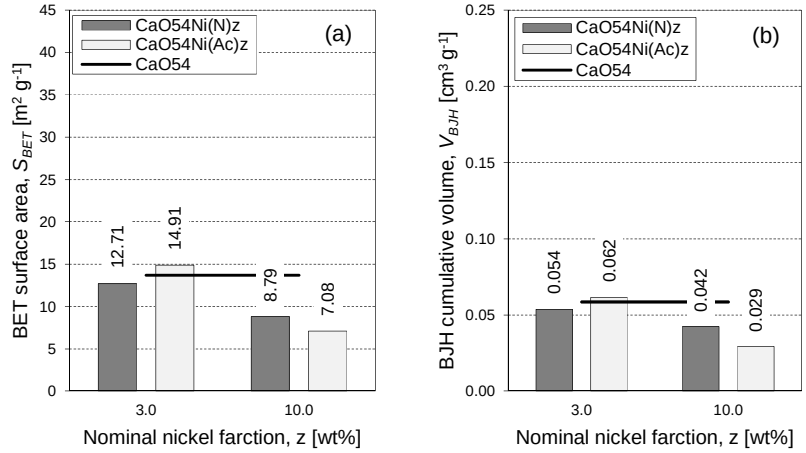

Figure 8: (a) BET surface areas (S_{BET}) and (b) BJH cumulative volumes (V_{BJH}) for CSCM with corresponding CaO54 values as a reference.

As far as CSCM are concerned, the presence of free CaO fraction in CaO54 led to a reverse trend to that observed in the absence of free CaO fraction (CaO0 samples), regardless of Ni fraction and its origin. In fact, after wet impregnation of CaO54 to obtain 3 wt% or 10% of Ni, S_{BET} (Figure 8a) and V_{BJH} (Figure 8b) slightly decreased from values shown by CaO54, with the exception of CaO54Ni(Ac)3; wet impregnation by Ni(Ac) gave slightly higher S_{BET} and V_{BJH} than those by Ni(N). However, in these comparisons, it is worth to remark that the Ca/Al ratio (Table 3) is the highest for CaO54Ni(Ac)3 sample and the lowest for CaO54Ni(Ac)10 sample.

3.1.6 Reduction properties

H_2 consumption profiles during TPR for Ni-mayenite SMR catalysts (Figure 9) showed several kinds of reduction peaks. Ni(N) derived catalysts (Figure 9a) exhibited their main peaks at temperatures higher than 800 °C, then related to $NiAl_2O_4$ spinel phase reduction by H_2 to metallic Ni and Al_2O_3 [59–63], the intensity of which grew with nominal Ni content; a left shoulder in the range 650-750 °C indicated the presence of Ni in strong interaction with the support structure [6,60,64]; peaks in the range 450-550 °C, representing NiO in moderate interaction with the support [63], and minor peaks from free NiO appeared in the region below 400 °C [62,65] were more and more relevant as Ni nominal fraction increased.

Ni(Ac) derived catalysts (Figure 9b) presented a different behaviour, having their main reduction peaks around 650 °C, the higher the Ni fraction the more intense the peak, with a right shoulder at 775-785 °C: these temperatures correspond to Ni in strong interaction with the support structure [6,60,63], but not in the form of $NiAl_2O_4$ spinel, to which only the smaller peaks at 910-915 °C could be related [62,63]; secondary peaks appeared, ascribable to NiO in moderate (485-510 °C) [64] and weak (400 °C or less) interactions with the support [62,65], similarly to Ni(N) derived catalysts.

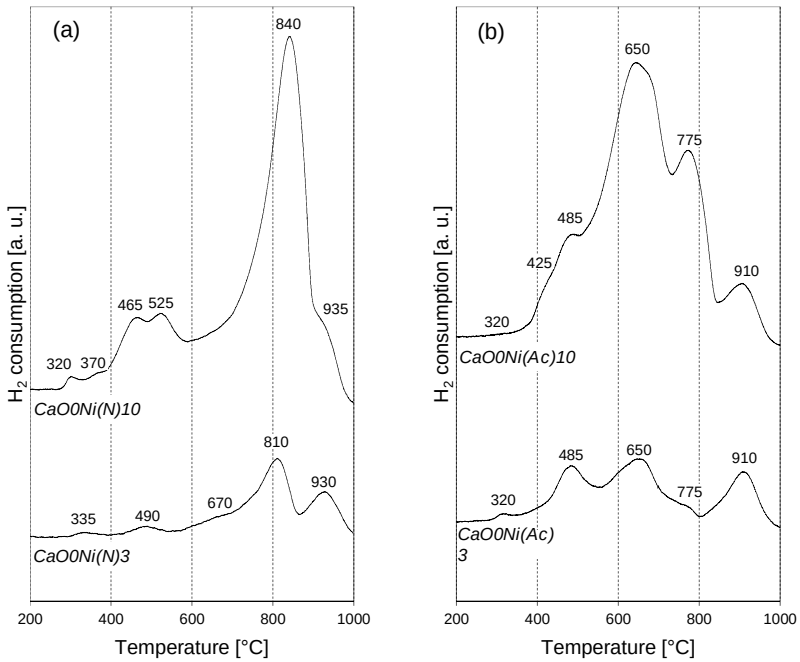

Figure 9: TPR profiles of Ni-mayenite SMR catalysts impregnated with (a) Ni(N) and (b) Ni(Ac); numbers on the curves represent the temperature (°C) at the maximum of the corresponding reduction peak.

TPR profiles of CSCM (Figure 10) showed influence on reducibility properties from nominal fractions of Ni and CaO and from Ni precursor salt. As far as wet impregnation by Ni(N) is concerned (Figure 10a), the CaO fraction of 54 wt% remarkably shifted the most intense reduction peaks towards lower temperature (500-650 °C, NiO species in strong interaction with CaO [6] or calcium aluminates [60]) when compared to the main peak (> 800 °C) of CaO0Ni(N)*z*, therefore evidencing weaker Ni-support interactions. For CaO54Ni(N)10, reduction arose just for NiO in weak (453 °C and 480 °C) [6,65] and stronger (625 °C and 695 °C) [60] interactions with the support.

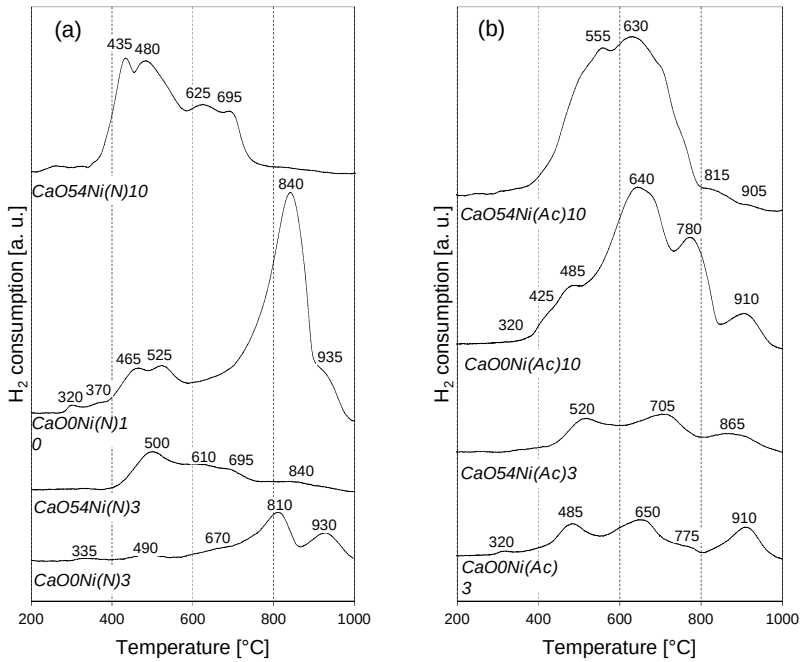

Figure 10: TPR profiles of CSCM impregnated with (a) Ni(N) and (b) Ni(Ac); numbers on the curves represent the temperature (°C) at the maximum of the corresponding reduction peak.

For Ni(Ac) samples (Figure 10b), CaO54Ni(Ac)*z* reduction peaks were in the same range of temperature than the CaO0Ni(Ac)*z* reduction peaks, highlighting the absence of free-CaO influence. The main peak, increasing with Ni fraction, is between 630 °C and 650 °C, due to NiO in strong interaction with CaO [6,59], with shoulders beyond 800 °C ascribable to $NiAl_2O_4$ [59–63].

It is worth stressing here that, in the above discussion of TPR results, high temperature peaks were attributed to $NiAl_2O_4$, even though this phase was not detected by XRD analyses on as-synthesized materials (Figure 1 1 and Figure 2). Nevertheless, the presence of this spinel as a surface species, although hardly detectable by XRD, is proposed in literature as a cause of high temperature peaks from TPR of supported Ni [59,60,62,64,66].

XRD analyses on Ni-mayenite SMR catalysts (Figure 11) and CSCM (Figure 12) after TPR confirmed the occurrence of NiO reduction to metallic Ni. Crystalline phases already present in as-synthesized materials were kept. $Ca(OH)_2$, occasionally found in samples after TPR (Figure 12), could be ascribed to CaO reactions with environmental moisture. Moreover, small traces of $Ca_3Al_2O_6$ (left shoulder on mayenite peak at $2\theta = 33$ °) and $CaAl_4O_7$ (peak at $2\theta = 25$ °) were sometimes detected. $Ca_3Al_2O_6$ is in equilibrium with mayenite for Ca/Al molar ratios higher than 6/7 and lower than 3, while $CaAl_4O_7$ equilibrates $CaAl_2O_4$ for Ca/Al molar ratios higher than 1/4 and lower than 1/2 [67]. TPR procedure nominally reached 1000 °C, therefore acted as an additional thermal treatment on as-synthesized samples, with the potentiality to provoke new solid state reactions; in fact, the formation of these new calcium aluminates could

be related to $Ca_{12}Al_{14}O_{33}$ instability in dry conditions at 1050 °C, temperature close to those of the TPR dwell [67], also considering that in the used TPR device (§2.3.6) the thermocouple was not within the active packed bed.

Ni-mayenite catalysts after TPR (Figure 11) presented both $Ca_3Al_2O_6$ and $CaAl_4O_6$ phases formed during reduction. For the same nominal Ni fraction, their XRD rays were more intense in Ni(Ac) derived materials. In both Ni(N) and Ni(Ac) families, intensity of Ni rays increased as Ni nominal fraction increased.

In CSCM after TPR (Figure 12), $Ca_3Al_2O_6$ was barely distinguishable only for samples with nominal 10 wt% of Ni. Tables 4 and 5 summarize average crystallite size estimates by Scherrer equation (Equation 1) for samples after TPR. For $Ca_{12}Al_{14}O_{33}$ and CaO phases, values are systematically higher, with the only exception of CaO54Ni(N)10, than those of the same materials in as-synthesized state, showing the occurrence of slight sintering phenomena because of TPR heating procedure. Values estimated for Ni phase crystallites, quite homogeneous among all samples (between 26 and 31 nm), were used as a reference to evaluate sintering occurrence in materials tested for SMR and SESMR.

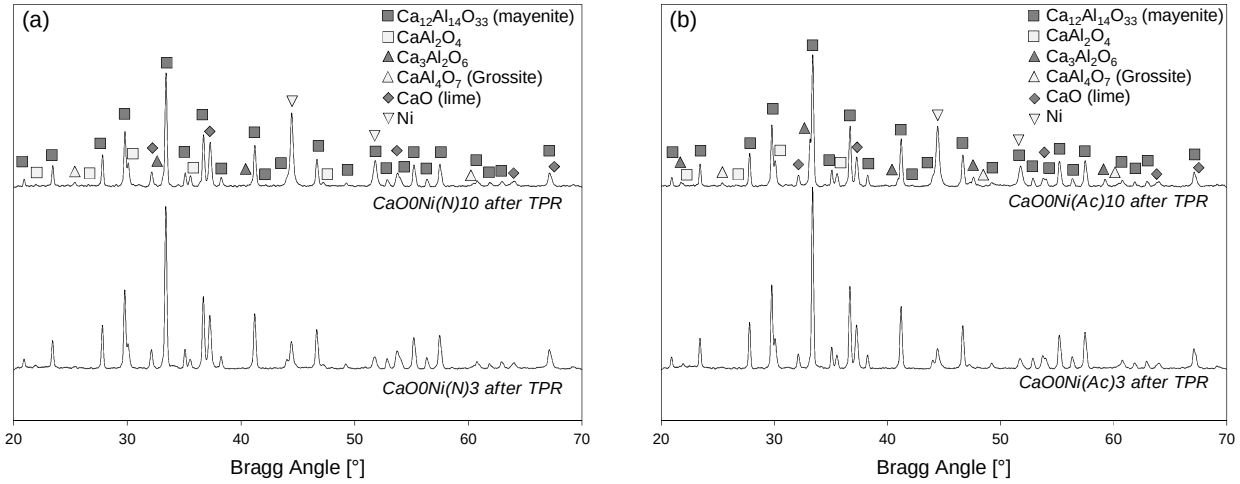

Figure 11: X-ray diffractograms of Ni-mayenite SMR catalyst, impregnated with (a) Ni(N) and (b) Ni(Ac), after TPR.

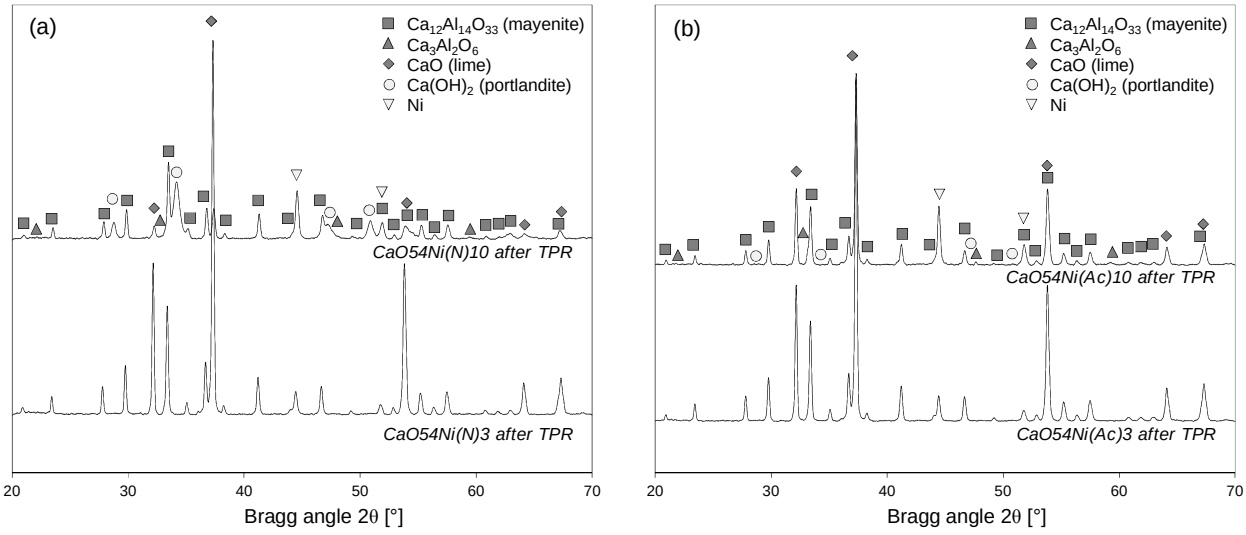

Figure 12: X-ray diffractograms of CaO54Ni(Y)z CSCM, impregnated with (a) Ni(N) and (b) Ni(Ac), after TPR.

3.2 Catalytic tests

3.2.1 Reference equilibrium compositions

Table 6 summarizes equilibrium values for SMR and SESMR, computed by CHEMCAD® 6.5 in [28], at operating conditions defined in §2.4.2 and §2.4.3. These values were used as a reference to evaluate reactive performances of tested materials.

Table 6: Equilibrium values for SMR and SESMR at different experimental conditions, calculated by CHEMCAD® 6.5 simulations; constant values are P = 1 atm, inlet steam to carbon molar ratio = 3, CaO/CH_4 molar ratio = 8.5 [28]

	T [°C]	Simulated $C_{i,out}$ [vol% dry diluent free]				Simulated
		CH_4	H_2	CO	CO_2	CH_4 conv. [%]
SMR	850	0.0	76.8	16.0	7.2	100.0
SMR	750	0.1	77.1	14.1	8.7	99.8
SMR	650	0.8	77.0	11.5	10.7	96.7
SESMR	650	0.1	97.9	0.4	1.6	99.4

3.2.2 Results of SMR tests

Table 7 summarizes SMR results from catalytic activity tests on Ni-mayenite materials. From the reactive point of view, very different χ_{CH4} were detected, depending on the Ni precursor salt.

Table 7: Experimental χ_{CH4} from reforming activity tests on Ni-mayenite materials, according to SMR-1 and SMR-2 procedures; WHSV = 0.24 Nl h^{-1} g_{bed}^{-1}; χ_{CH4} reported as a unique number results from the average of experimental measurements, χ_{CH4} as a range indicates the extreme values of a clearly increasing (↑) or decreasing (↓) trend

Material	Ni-WHSV [$Nl_{CH4,in}$ h^{-1} g_{Ni}^{-1}]		χ_{CH4} *in* SMR-1 [%]			χ_{CH4} *in* SMR-2 [%]
	Nominal	Actual	850 °C	750 °C	650 °C	650 °C
CaO0Ni(N)3	8.0	8.3	100.0	99.5	96.7	96.2
CaO0Ni(N)10	2.4	2.1	100.0	100.0	97.8	96.4
CaO0Ni(Ac)3	8.0	7.7	59.1 ↑ 92.6	40.1 ↑ 45.0	7.4	19.5 ↓ 4.3
CaO0Ni(Ac)10	2.4	2.4	81.7 ↑ 90.3	33.3 ↑ 37.3	5.9	10.2 ↓ 4.4

Figure 13 reports SMR results for Ni-mayenite catalysts from Ni(N). At a WHSV of 0.24 Nl h^{-1} g_{bed}^{-1}, their performances always stabilized around values very close to SMR equilibrium (Table 6 as reference), whatever the

nominal Ni fraction in the range from 3 wt% to 10 wt%. As far as SMR-1 is concerned, χ_{CH4} was complete at 850 °C (i.e. no CH_4 detectable downstream), almost complete at 750 °C, and with a further decrease of some percentage points at 650 °C. During the transition between 750 °C and 650 °C, $C_{H2,out}$ was temporary higher than its expected equilibrium value (Table 6 as reference), especially for CaO0Ni(N)3 (and CaO0Ni(N)4.5, not shown); this could be ascribed to a sorption enhancing effect due to residual CaO found in as-synthesized materials (Figure 1a). For each material, χ_{CH4} in SMR-1 at 650 °C was slightly higher than in SMR-2. This could be related to the different SMR triggering environments at 650 °C in the two cases: already developed H_2 in SMR-1 and only reactants (CH_4 and $H_2O_{(v)}$) diluted in Ar in SMR-2, the former being more reductive than the latter [28]. Another hypothesis is the ageing of catalysts.

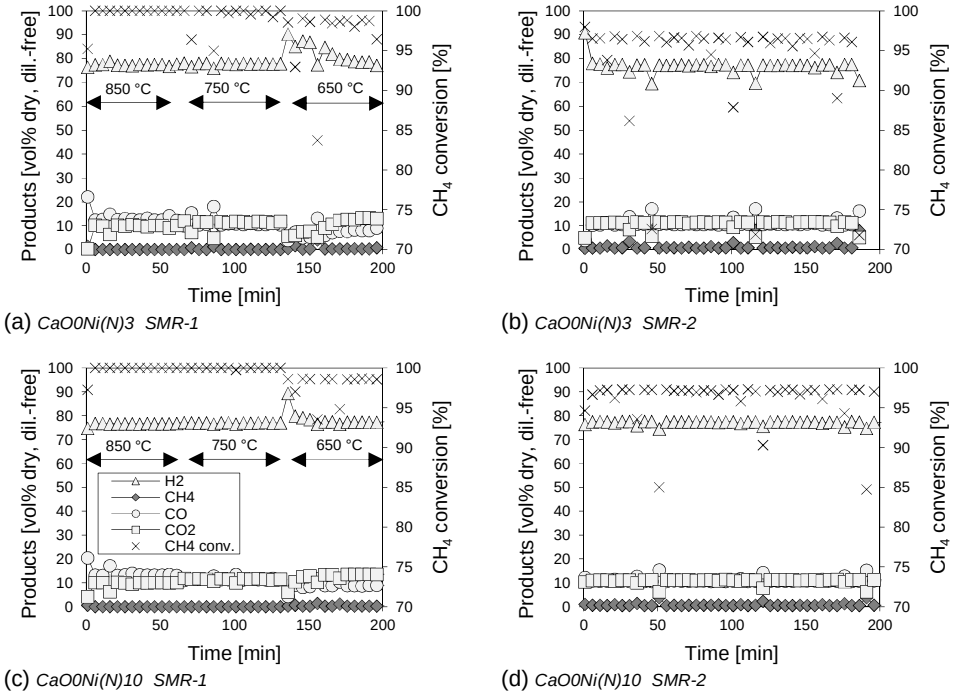

Figure 13: Results from reforming tests on (a, b) CaO0Ni(N)3, (c, d) CaO0Ni(N)10. Left column: SMR-1 procedure; Right column: SMR-2 procedure. Legend in (c) is valid for all diagrams.

The situation radically changed for Ni-mayenite SMR catalysts from Ni(Ac) (Figure 14). At the same WHSV of 0.24 Nl h^{-1} g_{bed}^{-1}, they generally showed a dramatic decrease of SMR catalytic activity in comparison with materials from Ni(N) (Table 7), very far from SMR equilibrium achievement (Table 6 as reference). In SMR-1 experiments, for the two Ni(Ac) catalysts, a kind of apparent systematic self-activation occurred at 850 °C and 750 °C, as can be seen by χ_{CH4} increasing trends (Figure 14a, Figure 14c); this could be related to the conversion of carbonaceous deposits by gasification reactions with steam. In fact, carbonaceous deposit was observed on as-synthesized samples (Figure 6) but is mainly produced during the activation of the catalyst by Boudouard reactions (CO and CO_2 formation).

The influence of temperature (Figure 14) was considerable: χ_{CH4} reached values higher than 90 % at 850 °C, passed through a range between 33 % and 46 % at 750 °C, and eventually got to less than 8 % at 650 °C. It is worth stressing here that all tested materials underwent the same pre-reduction process (§2.4.2) and that, before the end of its final step at 900 °C, H_2 consumption always ended to zero for all reported materials, confirming the occurrence of the maximum Ni reduction achievable at operating conditions. As far as SMR-2 is concerned (Figure 14b and Figure 14d), all Ni-mayenite catalysts from Ni(Ac) exhibited the same behaviour: an initial attempt of reaction, with an exponential decrease towards χ_{CH4} lower than those obtained according to SMR-1 procedure at 650 °C.

In Ni(Ac) catalysts compared to Ni(N) catalysts, Ni content has also an opposite influence on catalyst efficiency. The higher the Ni content, the lower the χ_{CH4} during SME-1 procedure (temperature evolution) and the lower the H_2 content at a given temperature. Then the higher the Ni content, the greater the catalyst deactivation thus linked to Ni sintering.

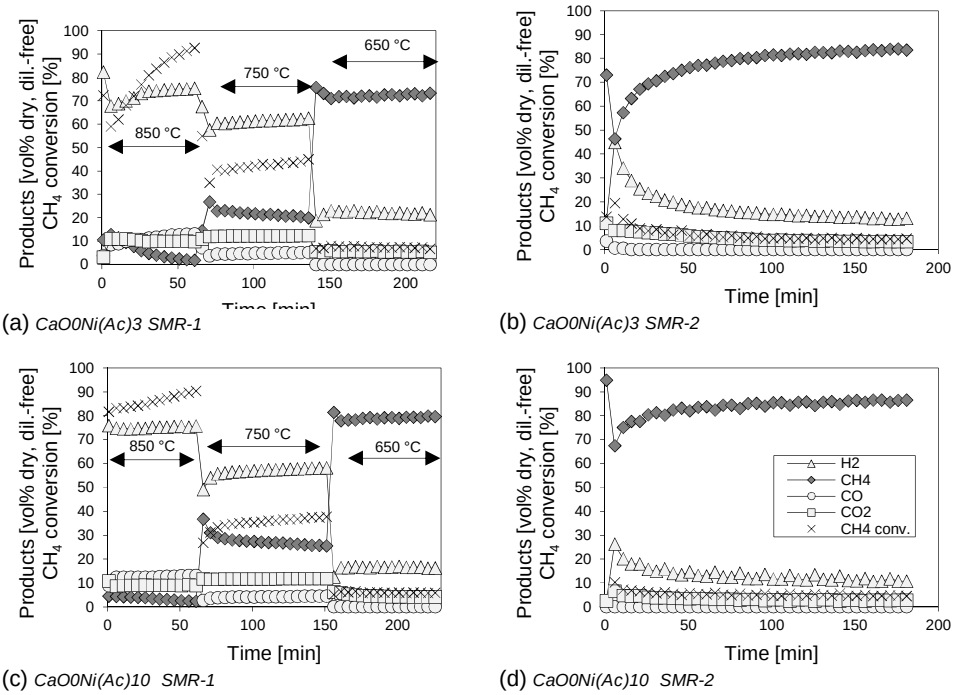

Figure 14: Results from reforming tests on (a, b) CaO0Ni(Ac)3, (c, d) CaO0Ni(Ac)10. Left column: SMR-1 procedure; Right column: SMR-2 procedure. Legend in (d) is valid for all diagrams.

The behavior difference observed for Ni(N) and Ni(Ac) catalysts in SMR reactivity can be explained by several characterizations data:

- Higher NiO crystallites size in as-synthesized catalysts were reported (Table 5) at the same Ni content, particularly for z = 10;

- A better NiO dispersion on mayenite matrix in CaO0Ni(N)10 than in CaO0Ni(Ac)10 was evidenced by TEM (Figure 5) ensuring Ni(N) catalyst stability;
- A carbonaceous matrix in Ca0Ni(Ac)10 catalyst was observed by TEM around NiO crystallites (Figure 6) limiting the accessibility of Ni crystallites by CH_4;
- Lower S_{BET} and V_{BJH} were measured for Ni(Ac) compared to Ni(N) catalysts (Figure 7) also reducing the gas-solid contact;
- A reducibility of Ni(Ac) catalysts at lower temperature than Ni(N) catalysts (Figure 9) increasing the sintering risk.

3.2.3 Characterization of Ni-mayenite materials after SMR tests

After reforming tests documented in §3.2.2, Ni-mayenite materials were examined by XRD (Figure 15). For both Ni(N) (Figure 15a) and Ni(Ac) (Figure 15b) derived materials, Ni was detected only in its metallic state, formed by pre-reduction operated at the beginning of each test (§2.4.1). No NiO was detected in after-test samples (Figure 15), so no bulk re-oxidation of catalytic phase occurred.

Formation of $CaCO_3$ in Ni-mayenite from Ni(N) was observed (Figure 15a), in agreement with observed occurrence of sorption enhancing during the cooling phase between 750 °C and 650 °C. No formation of $CaCO_3$ in Ni-mayenite from Ni(Ac) was observed (Figure 15b) confirming the absence of CO_2 sorption on these materials because of the low CO_2 partial pressure at the catalyst surface. No other relevant structural variation was detected by comparison with materials in their as-synthesized state (Figure 1).

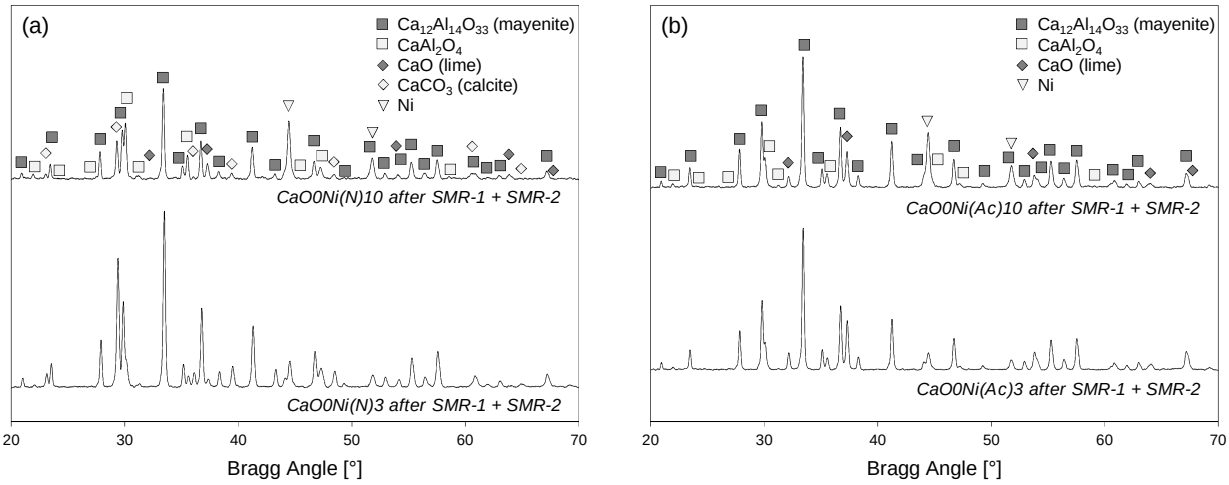

Figure 15: X-ray diffractograms for Ni-mayenite SMR catalysts impregnated with (a) Ni(N) and (b) Ni(Ac), after reforming tests by SMR-1 and SMR-2 procedures.

Tables 4 and 5 report results of *L* estimates by Scherrer equation (Equation 1) for Ni-mayenite materials after SMR catalytic reforming tests. For $Ca_{12}Al_{14}O_{33}$, *L* were systematically higher than those in the as-synthesized state, evidencing the occurrence of a slight sintering process, similarly to that detected for TPR (Table 4) and more intense for CaO0Ni(Ac)3. The same consideration was valid for unconverted residual CaO in Ni(Ac) catalysts with the same specificity for CaO0Ni(Ac)3. This sintering phenomena of mayenite and unconverted CaO can be responsible for lower reactivity observed with Ni(Ac) catalysts. Metallic Ni diameters (Table 5) were quite similar to those obtained after TPR, so the catalytic active phase did not undergo severe sintering within the reaction environment. Then, mayenite and CaO phases would have an indirect catalytic effect in SMR thanks to the easy access of Ni sites resulting from proper distribution of Ni on the substrate as previously reported [34].

TEM micrographs of CaO0Ni(N)10 and CaO0Ni(Ac)10 after reforming tests are shown in Figure 16. Dark spheroidal particles were metallic Ni, as inferred by cross-correlating STEM-EDS elemental analyses detecting elemental Ni and XRD spectra locating metallic Ni as the only Ni-containing phase (Figure 11). The main difference between the catalysts prepared from various Ni precursors was in the developing of proto-filamentous, carbonaceous structures nearby these Ni particles in CaO0Ni(N)10 after SMR, but not in CaO0Ni(Ac)10 (Figure 16, 20 nm magnifications); the presence of elemental carbon in CaO0Ni(N)10 was confirmed by STEM-EDS. Based on experimental reforming results (Table 7), the presence of carbon on the former catalyst can be related to its activity.

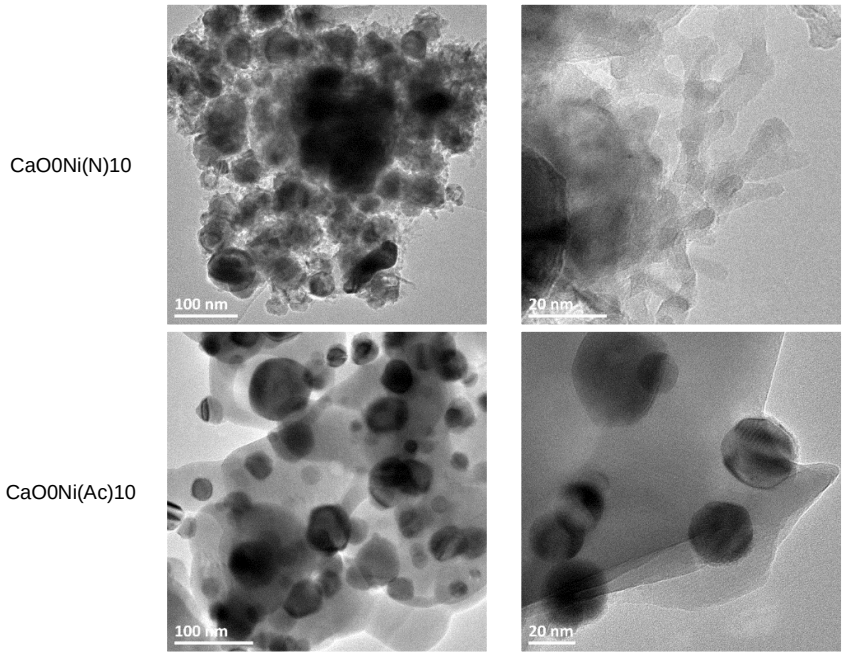

Figure 16: TEM micrographs of CaO0Ni(N)10 (first row) and CaO0Ni(Ac)10 (second row) after reforming tests by SMR-1 and SMR-2 procedures.

Finally, Ni(N) catalysts were able to fully develop SMR (Figure 13) and CaO0Ni(N)10 was capable to maintain total methane conversion (χ_{CH4}) even at 650 °C (Figure 13c). Ni(Ac) catalysts were very less reactive (Figure 14), and no longer of interest at 650 °C to be considered as CSCM for simultaneous CO_2 sorption.

3.2.4 Results of SESMR tests

Table 8 summarizes results from reforming activity tests on CSCM, where sorption enhancing duration (t^*) was empirically located among sampling test times (t), by means of $C_{H2,out}$ and $C_{CO2,out}$ stabilization, related to sorbent saturation.

Ni fraction and therefore Ni-WHSV played a relevant role on reactive performances in CaO54Ni(N)z samples: 3wt% of Ni is not enough to totally convert methane or to maintain the initial conversion. Because of its rapid deactivation it was quite difficult to infer whether some sorption enhancing occurred or not.

Table 8: Experimental χ_{CH4} from reforming activity tests on Ni-CaO-mayenite CSCM; WHSV = 0.24 Nl h^{-1} g_{bed}^{-1}; χ_{CH4} as a unique number results from the average of experimental measurements, ranged χ_{CH4} indicates the extreme values of a clearly increasing (↑) or decreasing (↓) trend.

CSCM	**Ni-WHSV [$Nl_{CH4,i}$ h^{-1} g_{Ni}^{-1}]**		***t***[min]*	χ_{CH4} **[%]**		
	Nominal	**Actual**		$t \leq t^*$	$t > t^*$	**Overall**
CaO54Ni(N)3	8.0	10.0	/	/	/	39.5 ↓ 10.2
CaO54Ni(N)10	2.4	2.6	76	96.8	96.7	96.8
CaO54Ni(Ac)3	8.0	9.6	/	/	/	0.0
CaO54Ni(Ac)10	2.4	2.4	/	/	/	0.6

On the other hand, for CaO54Ni(N)10, SMR was stably sustained throughout the whole test duration, with χ_{CH4} beyond 96 %, allowing the sorption enhancing effect in the first part, with initial $C_{H2,out}$ equal to about 90 vol% dry, diluent free. The performances comparison of CaO54 and CaO0 (Table 7) derived materials highlights a detrimental role of CaO fraction increase on Ni reactivity in CSCM, particularly for low Ni content, as already concluded in [28].

The results for CaO54Ni(Ac)z samples (Table 8) are as expected and confirm the effect of Ni precursor: their reactivity was almost (for CaO54Ni(Ac)10) or entirely zero (for CaO54Ni(Ac)3).

Additionally, the effects of in-situ CO_2 capture (i.e. sorption enhancing) on H_2 concentration are clearly visible until t* for CaO54Ni(N)10 (Figure 17b), as well as already described worse performances of other CSCM (Figure 18).

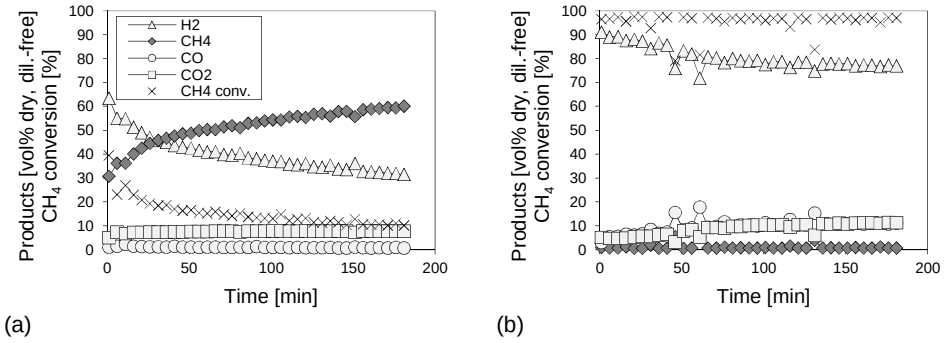

Figure 17: Results from reforming tests on CSCM from Ni(N): (a) CaO54Ni(N)3, (b) CaO54Ni(N)10; legend in (a) is valid for all diagrams.

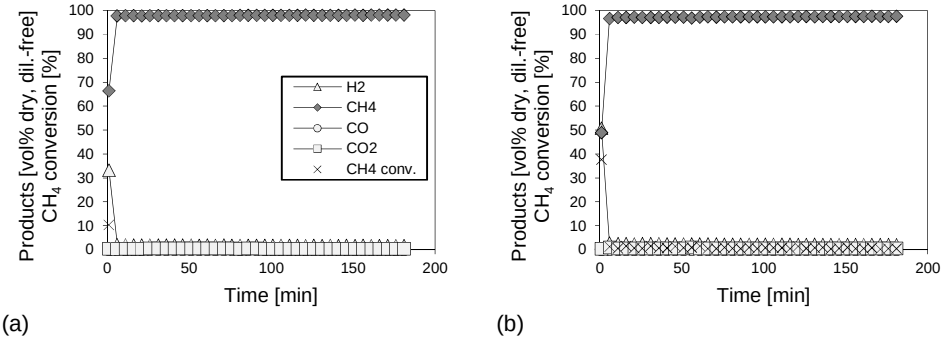

Figure 18: Results from reforming tests on CSCM from Ni(Ac): (a) CaO54Ni(Ac)3, (b) CaO54Ni(Ac)10); legend in (a) is valid for all diagrams.

3.2.5 Characterization after SESMR tests

By XRD, CaO54Ni(N)3 and CaO54Ni(N)10 after reforming tests showed the formation of $CaCO_3$ with a concomitant relevant decrease of CaO rays intensity, in comparison to the same CSCM in as-synthesized state (Figure 2a), so corroborating the occurrence of carbonation (Reaction 3) and therefore of SESMR. $CaCO_3$ appeared less intensely in CaO54Ni(N)3, while CaO rays persisted more strongly, in accordance with observed reforming experimental results revealing a scarce but not negligible reactivity (Table 8), sufficient to produce enough CO_2 to trigger a partial CaO carbonation (Reaction 3). The $CaCO_3$ particle size (Table 4) was similar after SESMR (CaO54Ni(N)z) than after SMR (CaO0Ni(N)z) despite the sorbent saturation in SESMR tests. Metallic Ni, formed during the pre-reduction step, was kept during the 3 h SESMR session for all Ni(N) derived CSCM.

The unique phase variation of CSCM derived from Ni(Ac) in comparison to their as-synthesized state (Figure 2b) was the emergence of metallic Ni, as a consequence of pre-reduction. Moreover, traces of NiO appeared most likely because of Ni exposure to SESMR reactants (CH_4 and $H_2O_{(v)}$) for 3 h. No $CaCO_3$ was detected, in accordance with the absence of sufficient reforming reactivity (Table 8).

4 Conclusions

As far as Ni-mayenite properties are concerned, the variation of Ni precursor salt and its fraction in wet impregnated samples mainly affected the textural and reducibility properties. S_{BET} and V_{BJH} of Ni-mayenite decreased as the final Ni fraction increased, more dramatically in the case of Ni(Ac) samples. TPR profiles evidenced that Ni species in Ni-mayenite deriving from Ni(N) had more intense interaction than that in Ni(Ac) ones; in both families, as Ni fraction increases, the specific kind of the main interaction remains unchanged. A higher integration with the support of Ni derived from Ni(N) than that from Ni(Ac) was also observed by TEM.

With regard to CSCM properties, effects from Ni precursor salt and its fraction were modified by those from "free" CaO fraction (54 wt%).

As far as Ni-mayenite SMR reactivity is concerned, the main feature was a clear distinction between Ni(N) and Ni(Ac) derivation: Ni(N) derived catalysts determined a high SMR reactivity at WHSV equal to 0.24 $Nl_{CH4,in}\ h^{-1}\ g_{bed}^{-1}$, whatever the nominal Ni fraction between 3 wt% and 10 wt% and the tested temperature; on the other hand, Ni(Ac) derived catalysts had worse performances than those exhibited by Ni(N) at the same operating conditions, especially unsatisfactory at 650 °C, the temperature of interest for SESMR. Characterization results from Ni-mayenite after SMR did not give significant signals of Ni(Ac) catalysts deterioration because of low activity. The sintering of mayenite and CaO phases seems to be important in the explanation of Ni(Ac) catalysts inefficiency.

Similarly, CSCM deriving from Ni(N) with nominal 10 wt% of Ni, i.e. nominal Ni-WHSV equal to 2.4 $Nl_{CH4,in}\ h^{-1}\ g_{Ni}^{-1}$, exhibited a satisfying catalytic activity, higher than that of its homologue from Ni(Ac), whose catalytic activity was almost zero. SESMR and SMR were developed and sustained only by Ni(N) derived CSCM, the higher the Ni fraction the higher the reactivity.

As a conclusion, for the success in steam methane reforming and sorption enhanced steam reforming, Ni-mayenite and Ni-CaO-mayenite materials synthesized by wet mixing and wet impregnation with nickel nitrate, labelled as Ni(N), are definitely more appropriate than their corresponding Ni(Ac) counterparts.

5 Nomenclature

5.1 Symbols

C_i	volumetric concentration of *i*, on dry and free diluent basis [$\%_v$ on dry and free diluent basis]
cGG_i	volumetric concentration of *i*, measured by GC [vol% on dry basis]

d_p particle diameter [µm]

F_i molar flowrate of *i* [Nml min^{-1} ; Nl h^{-1}]

m sample mass [g]

w_{Ni} nominal weight fraction of nickel [wt%]

5.2 Subscripts

bed packed bed in SMR/SESMR experimental apparatus

i gaseous component (N_2, CH_4, H_2, CO, CO_2)

in inlet

out outlet

6 Acknowledgements

The research leading to these results has received funding from the European Union's Seventh Framework Program ASCENT grand agreement n° [608512].Authors kindly thank Corinne Bouillet (ICPMS) for STEM analyses and Lorenzo Arrizza (CEM) for SEM analyses.

7 Bibliography

[1] J.S. Wallace, C.A. Ward, Hydrogen as a fuel, Int. J. Hydrogen Energy. 8 (1983) 255–268. doi:10.1016/0360-3199(83)90136-2.

[2] T.N. Vezirolu, F. Barbir, Hydrogen: the wonder fuel, Int. J. Hydrogen Energy. 17 (1992) 391–404. doi:10.1016/0360-3199(92)90183-W.

[3] D.C. Miller, J.T. Litynski, L.A. Brickett, B.D. Morreale, Toward transformational carbon capture systems, AIChE J. 62 (2016) 2–10. doi:10.1002/aic.15066.

[4] J.D. Holladay, J. Hu, D.L. King, Y. Wang, An overview of hydrogen production technologies, Catal. Today. 139 (2009) 244–260. doi:10.1016/j.cattod.2008.08.039.

[5] R. Kothari, D. Buddhi, R.L. Sawhney, Comparison of environmental and economic aspects of various hydrogen production methods, Renew. Sustain. Energy Rev. 12 (2008) 553–563. doi:10.1016/j.rser.2006.07.012.

[6] M.R. Cesário, B.S. Barros, C. Courson, D.M.A. Melo, A. Kiennemann, Catalytic performances of Ni-CaO-mayenite in CO_2 sorption enhanced steam methane reforming, Fuel Process. Technol. 131 (2015) 247–253. doi:10.1016/j.fuproc.2014.11.028.

[7] M.H. Halabi, M.H.J.M. de Croon, J. van der Schaaf, P.D. Cobden, J.C. Schouten, A novel catalyst–sorbent system for an efficient H_2 production with in-situ CO_2 capture, Int. J. Hydrogen Energy. 37 (2012) 4987–4996. doi:10.1016/j.ijhydene.2011.12.025.

[8] W. Wang, Y. Cao, Hydrogen production via sorption enhanced steam reforming of butanol: Thermodynamic analysis, Int. J. Hydrogen Energy. 36 (2011) 2887–2895. doi:10.1016/j.ijhydene.2010.11.110.

[9] T. da Silva Veras, T.S. Mozer, D. da Costa Rubim Messeder dos Santos, A. da Silva César, Hydrogen: Trends, production and characterization of the main process worldwide, Int. J. Hydrogen Energy. 42 (2017) 2018–2033. doi:10.1016/j.ijhydene.2016.08.219.

[10] A.B. Stambouli, E. Traversa, Solid oxide fuel cells (SOFCs): A review of an environmentally clean and efficient source of energy, Renew. Sustain. Energy Rev. 6 (2002) 433–455. doi:10.1016/S1364-0321(02)00014-X.

[11] O.Z. Sharaf, M.F. Orhan, An overview of fuel cell technology: Fundamentals and applications, Renew. Sustain. Energy Rev. 32 (2014) 810–853. doi:10.1016/j.rser.2014.01.012.

[12] V. Das, S. Padmanaban, K. Venkitusamy, R. Selvamuthukumaran, F. Blaabjerg, P. Siano, Recent advances and challenges of fuel cell based power system architectures and control – A review, Renew. Sustain. Energy Rev. 73 (2017) 10–18. doi:10.1016/j.rser.2017.01.148.

[13] J. Alazemi, J. Andrews, Automotive hydrogen fuelling stations: An international review, Renew. Sustain. Energy Rev. 48 (2015) 483–499. doi:10.1016/j.rser.2015.03.085.

[14] Toyota Motor Company, Hydrogen Fuel Cell Car | Toyota Mirai, (n.d.). https://ssl.toyota.com/mirai/fcv.html (accessed September 18, 2017).

[15] 2017 Clarity Fuel Cell – Environmentally-Conscious Vehicles | Honda, (n.d.). https://automobiles.honda.com/clarity-fuel-cell (accessed September 18, 2017).

[16] ix35 Fuel Cell Highlights | Eco Cars - Hyundai Worldwide, (n.d.). https://www.hyundai.com/worldwide/en/eco/ix35-fuelcell/highlights (accessed September 18, 2017).

[17] K. Liu, C. Song, V. Subramani, Hydrogen and syngas production and purification technologies, John Wiley & Sons, Inc. Publications, 2010. doi:10.1002/9780470561256.fmatter.

[18] R. Chaubey, S. Sahu, O.O. James, S. Maity, A review on development of industrial processes and emerging techniques for production of hydrogen from renewable and sustainable sources, Renew. Sustain. Energy Rev. 23 (2013) 443–462. doi:10.1016/j.rser.2013.02.019.

[19] International Energy Agency, Hydrogen Production and Storage. R&D Priorities and Gaps, Hydrog.

Implement. Agreem. 13 (2006) 392–392. doi:10.1016/0360-3199(88)90106-1.

[20] M. Broda, V. Manovic, Q. Imtiaz, A.M. Kierzkowska, E.J. Anthony, C.R. Müller, High-Purity Hydrogen via the Sorption-Enhanced Steam Methane Reforming Reaction over a Synthetic CaO-Based Sorbent and a Ni Catalyst, Environ. Sci. Technol. 47 (2013) 6007–6014. doi:10.1021/es305113p.

[21] L. Barelli, G. Bidini, F. Gallorini, S. Servili, Hydrogen production through sorption-enhanced steam methane reforming and membrane technology: A review, Energy. 33 (2008) 554–570. doi:10.1016/j.energy.2007.10.018.

[22] E. Simsek, A.K. Avci, Z.I. Önsan, Investigation of catalyst performance and microstructured reactor configuration for syngas production by methane steam reforming, Catal. Today. 178 (2011) 157–163. doi:10.1016/j.cattod.2011.08.021.

[23] U. Izquierdo, V.L. Barrio, J.F. Cambra, J. Requies, M.B. Güemez, P.L. Arias, G. Kolb, R. Zapf, A.M. Gutiérrez, J.R. Arraibi, Hydrogen production from methane and natural gas steam reforming in conventional and microreactor reaction systems, Int. J. Hydrogen Energy. 37 (2012) 7026–7033. doi:10.1016/j.ijhydene.2011.11.048.

[24] A. Boyano, A.M. Blanco-Marigorta, T. Morosuk, G. Tsatsaronis, Exergoenvironmental analysis of a steam methane reforming process for hydrogen production, Energy. 36 (2011) 2202–2214. doi:10.1016/j.energy.2010.05.020.

[25] L. Di Felice, C. Courson, P.U. Foscolo, A. Kiennemann, Iron and nickel doped alkaline-earth catalysts for biomass gasification with simultaneous tar reformation and CO_2 capture, Int. J. Hydrogen Energy. 36 (2011) 5296–5310. doi:10.1016/j.ijhydene.2011.02.008.

[26] M.R. Cesário, B.S. Barros, Y. Zimmermann, C. Courson, D.M.A. Melo, A. Kiennemann, CO_2 Sorption Enhanced Steam Reforming of Methane Using Ni/CaO · $Ca_{12}Al_{14}O_{33}$ Catalysts, Adv. Chem. Lett. 1 (2013) 292–299. doi:10.1166/acl.2013.1037.

[27] D.P. Harrison, Sorption-Enhanced Hydrogen Production: A Review, Ind. Eng. Chem. Res. 47 (2008) 6486–6501. doi:10.1021/ie800298z.

[28] A. Di Giuliano, J. Girr, R. Massacesi, K. Gallucci, C. Courson, Sorption enhanced steam methane reforming by Ni–CaO materials supported on mayenite, Int. J. Hydrogen Energy. 42 (2017) 13661–13680. doi:10.1016/j.ijhydene.2016.11.198.

[29] R.K. Pachauri, M.R. Allen, V.R. Barros, J. Broome, W. Cramer, R. Christ, J.A. Church, L. Clarke, Q. Dahe, P. Dasgupta, N.K. Dubash, O. Edenhofer, I. Elgizouli, C.B. Field, P. Forster, P. Friedlingstein, J. Fuglestvedt, L.

Gomez-Echeverri, S. Hallegatte, G. Hegerl, M. Howden, K. Jiang, B. Jimenez Cisneroz, V. Kattsov, H. Lee, K.J. Mach, J. Marotzke, M.D. Mastrandrea, L. Meyer, J. Minx, Y. Mulugetta, K. O'Brien, M. Oppenheimer, J.J. Pereira, R. Pichs-Madruga, G.-K. Plattner, H.-O. Pörtner, S.B. Power, B. Preston, N.H. Ravindranath, A. Reisinger, K. Riahi, M. Rusticucci, R. Scholes, K. Seyboth, Y. Sokona, R. Stavins, T.F. Stocker, P. Tschakert, D. van Vuuren, J.-P. van Ypserle, Climate Change 2014: Synthesis Report. Contribution of Working Groups I, II and III to the Fifth Assessment Report of the Intergovernmental Panel on Climate Change, Epic. Switzerland, IPCC, 151 p., Pp. 151, ISBN 978-92-9169-143-2. (2014).

[30] United Nations, Paris Agreement, 21st Conf. Parties. (2015) 3. doi:FCCC/CP/2015/L.9.

[31] J.A. Satrio, B.H. Shanks, T.D. Wheelock, Development of a novel combined catalyst and sorbent for hydrocarbon reforming, Ind. Eng. Chem. Res. 44 (2005) 3901–3911. doi:10.1021/ie040284m.

[32] B.T. Carvill, J.R. Hufton, M. Anand, S. Sircar, Sorption-enhanced reaction process, AIChE J. 42 (1996) 2765–2772. doi:10.1002/aic.690421008.

[33] G.-H. Xiu, P. Li, A.E. Rodrigues, Sorption-enhanced reaction process with reactive regeneration, Chem. Eng. Sci. 57 (2002) 3893–3908. doi:10.1016/S0009-2509(02)00245-2.

[34] M. Shokrollahi Yancheshmeh, H.R. Radfarnia, M.C. Iliuta, High temperature CO_2 sorbents and their application for hydrogen production by sorption enhanced steam reforming process, Chem. Eng. J. 283 (2016) 420–444. doi:10.1016/j.cej.2015.06.060.

[35] C.S. Martavaltzi, E.P. Pampaka, E.S. Korkakaki, A.A. Lemonidou, Hydrogen Production via Steam Reforming of Methane with Simultaneous CO_2, Chem. Eng. J. 33 (2010) 2589–2595. doi:10.1021/ef9014058.

[36] J. Meyer, J. Mastin, C. Sanz, Sustainable Hydrogen Production from Biogas Using Sorption-Enhanced Reforming, Energy Procedia. 63 (2014) 6800–6814. doi:10.1016/j.egypro.2014.11.714.

[37] J. Meyer, J. Mastin, T.K. Bjørnebøle, T. Ryberg, N. Eldrup, Techno-economical study of the Zero Emission Gas power concept, in: Energy Procedia, Elsevier, 2011: pp. 1949–1956. doi:10.1016/j.egypro.2011.02.075.

[38] Bo Feng, H. An, and Eddie Tan, Screening of CO_2 Adsorbing Materials for Zero Emission Power Generation Systems, Energy & Fuels. 21 (2007) 426–434. doi:10.1021/ef0604036.

[39] A. Di Giuliano, K. Gallucci, Sorption enhanced steam methane reforming based on nickel and calcium looping: a review, Chemical Engineering and Processing - Process Intensification. 130 (2018) 240-252 . doi:10.1016/j.cep.2018.06.021.

[40] A.L. García-Lario, M. Aznar, I. Martinez, G.S. Grasa, R. Murillo, Experimental study of the application of a $NiO/NiAl_2O_4$ catalyst and a CaO-based synthetic sorbent on the Sorption Enhanced Reforming process, Int. J.

Hydrogen Energy. 40 (2015) 219–232. doi:10.1016/j.ijhydene.2014.10.033.

[41] N. Chanburanasiri, A.M. Ribeiro, A.E. Rodrigues, A. Arpornwichanop, N. Laosiripojana, P. Praserthdam, S. Assabumrungrat, Hydrogen Production via Sorption Enhanced Steam Methane Reforming Process Using Ni/CaO Multifunctional Catalyst, Ind. Eng. Chem. Res. 50 (2011) 13662–13671. doi:10.1021/ie201226j.

[42] C.S. Martavaltzi, A.A. Lemonidou, Hydrogen production via sorption enhanced reforming of methane: Development of a novel hybrid material-reforming catalyst and CO_2 sorbent, Chem. Eng. Sci. 65 (2010) 4134–4140. doi:10.1016/j.ces.2010.04.038.

[43] J.-N. Kim, C.H. Ko, K.B. Yi, Sorption enhanced hydrogen production using one-body CaO–$Ca_{12}Al_{14}O_{33}$–Ni composite as catalytic absorbent, Int. J. Hydrogen Energy. 38 (2013) 6072–6078. doi:10.1016/j.ijhydene.2012.12.022.

[44] E. Marceau, M. Che, J. Čejka, A. Zukal, Nickel(II) Nitrate vs. Acetate: Influence of the Precursor on the Structure and Reducibility of Ni/MCM-41 and Ni/Al-MCM-41 Catalysts, ChemCatChem. 2 (2010) 413–422. doi:10.1002/cctc.200900289.

[45] J. Estellé, P. Salagre, Y. Cesteros, M. Serra, F. Medina, J.E. Sueiras, Comparative study of the morphology and surface properties of nickel oxide prepared from different precursors, Solid State Ionics. 156 (2003) 233–243. doi:10.1016/S0167-2738(02)00612-4.

[46] S.B. Ren, J.H. Qiu, C.Y. Wang, B.L. Xu, Y.N. Fan, Y. Chen, Influence of nickel salt precursors on the hydrogenation activity of Ni/gamma-Al2O3 catalyst, Chinese J. Catal. 28 (2007) 651–656. doi:10.1016/S1872-2067(07)60056-4.

[47] G. Wu, C. Zhang, S. Li, Z. Han, T. Wang, X. Ma, J. Gong, Hydrogen production via glycerol steam reforming over Ni/Al_2O_3: Influence of nickel precursors, ACS Sustain. Chem. Eng. 1 (2013) 1052–1062. doi:10.1021/sc400123f.

[48] A. Monshi, Modified Scherrer Equation to Estimate More Accurately Nano-Crystallite Size Using XRD, World J. Nano Sci. Eng. 02 (2012) 154–160. doi:10.4236/wjnse.2012.23020.

[49] J.I. Langford, A.J.C. Wilson, Scherrer after sixty years: A survey and some new results in the determination of crystallite size, J. Appl. Crystallogr. 11 (1978) 102–113. doi:10.1107/S0021889878012844.

[50] M. Xie, Z. Zhou, Y. Qi, Z. Cheng, W. Yuan, Sorption-enhanced steam methane reforming by in situ CO_2 capture on a CaO–$Ca_9Al_6O_{18}$ sorbent, Chem. Eng. J. 207–208 (2012) 142–150. doi:10.1016/j.cej.2012.06.032.

[51] C.S. Martavaltzi, T.D. Pefkos, A.A. Lemonidou, Operational window of sorption enhanced steam reforming of methane over CaO−$Ca_{12}Al_{14}O_{33}$, Ind. Eng. Chem. Res. 50 (2011) 539-545. doi:10.1021/ie1002284.

[52] A. Di Giuliano, K.Gallucci, F.Giancaterino, C.Courson, P. U.Foscolo, Multicycle sorption enhanced steam methane reforming with different sorbent regeneration conditions: experimental and modelling study, In press, Chem. Eng. J. - Available online 8 Sept. 2018. doi:10.1016/j.cej.2018.09.035.

[53] A. Di Giuliano, F. Giancaterino, K. Gallucci, P. U. Foscolo, C. Courson, Catalytic and sorbent materials based on mayenite for sorption enhanced steam methane reforming with different packed-bed configurations, Int. J. Hydrogen Energy, 43 (2018) 21279-21289. doi:10.1016/j.ijhydene.2018.10.003.

[54] A. Di Giuliano, F. Giancaterino, C. Courson, P. U. Foscolo, K. Gallucci, Development of a Ni-CaO-mayenite combined sorbent-catalyst material for multicycle sorption enhanced steam methane reforming, Fuel 234 (2018) 687-699. doi:10.1016/j.fuel.2018.07.071.

[55] I. Aloisi, A. Di Giuliano, A. Di Carlo, P. U. Foscolo, C. Courson, K. Gallucci, Sorption enhanced catalytic Steam Methane Reforming: Experimental data and simulations describing the behaviour of bi-functional particles, Chem. Eng. J. 314 (2017) 570-582. doi:10.1016/j.cej.2016.12.014.

[56] A.L. García-Lario, G.S. Grasa, R. Murillo, Performance of a combined CaO-based sorbent and catalyst on H_2 production, via sorption enhanced methane steam reforming, Chem. Eng. J. 264 (2015) 697–705. doi:10.1016/j.cej.2014.11.116.

[57] A.D. Clague, J. Donnet, T. Wang, J.C. Peng, A comparison of diesel engine soot with carbon black, Carbon N. Y. 37 (1999) 1553–1565. doi:10.1016/S0008-6223(99)00035-4.

[58] J.C. De Jesus, I. Gonzalez, A. Quevedo, T. Puerta, Thermal decomposition of nickel acetate tetrahydrate: an integrated study by TGA, QMS and XPS techniques, J. Mol. Catal. A: Chem., 228 (2005) 283–291. doi:10.1016/j.molcata.2004.09.065.

[59] J.R. Rostrup-Nielsen, Catalytic Steam Reforming, Catal. Sci. Technol. 5 (1984) 1–117. http://www.scopus.com/inward/record.url?eid=2-s2.0-0021158095&partnerID=40&md5=7183995ebfcff200d638d2d56ce6576d.

[60] P. Xu, Z. Zhou, C. Zhao, Z. Cheng, Ni/CaO-Al_2O_3 bifunctional catalysts for sorption-enhanced steam methane reforming, AIChE J. 60 (2014) 3547–3556. doi:10.1002/aic.14543.

[61] R. Villa, C. Cristiani, G. Groppi, L. Lietti, P. Forzatti, U. Cornaro, S. Rossini, Ni based mixed oxide materials for CH_4 oxidation under redox cycle conditions, J. Mol. Catal. A Chem. 204–205 (2003) 637–646. doi:10.1016/S1381-1169(03)00346-7.

[62] J.A.C. Dias, J.M. Assaf, Influence of calcium content in Ni/CaO/γ-Al_2O_3 catalysts for CO_2-reforming of methane, Catal. Today. 85 (2003) 59–68. doi:10.1016/S0920-5861(03)00194-9.

[63] C. Dueso, A. Abad, F. García-Labiano, L.F. De Diego, P. Gayán, J. Adánez, A. Lyngfelt, Reactivity of a NiO/Al_2O_3 oxygen carrier prepared by impregnation for chemical-looping combustion, Fuel. 89 (2010) 3399–3409. doi:10.1016/j.fuel.2010.03.043.

[64] A. Cabello, P. Gayán, F. García-Labiano, L.F. de Diego, A. Abad, M.T. Izquierdo, J. Ad?nez, Relevance of the catalytic activity on the performance of a $NiO/CaAl_2O_4$ oxygen carrier in a CLC process, Appl. Catal. B Environ. 147 (2014) 980–987. doi:10.1016/j.apcatb.2013.10.034.

[65] C.K.S. Choong, Z. Zhong, L. Huang, Z. Wang, T.P. Ang, A. Borgna, J. Lin, L. Hong, L. Chen, Effect of calcium addition on catalytic ethanol steam reforming of Ni/Al_2O_3: I. Catalytic stability, electronic properties and coking mechanism, Appl. Catal. A Gen. 407 (2011) 145–154. doi:10.1016/j.apcata.2011.08.037.

[66] A. Cimino, M. Lo Jacono, M. Schiavello, Structural, magnetic, and optical properties of nickel oxide supported on .eta.- and .gamma.-alumins, J. Phys. Chem. 75 (1971) 1044–1050. doi:10.1021/j100678a005.

[67] J.-P. Eufinger, A. Schmidt, M. Lerch, J. Janek, Novel anion conductors – conductivity, thermodynamic stability and hydration of anion- substituted mayenite-type cage compounds $C_{12}A_7$:X (X = O, OH, Cl, F, CN, S, N), Phys. Chem. Chem. Phys. 17 (2015) 6844–6857. doi:10.1039/C4CP05442C.

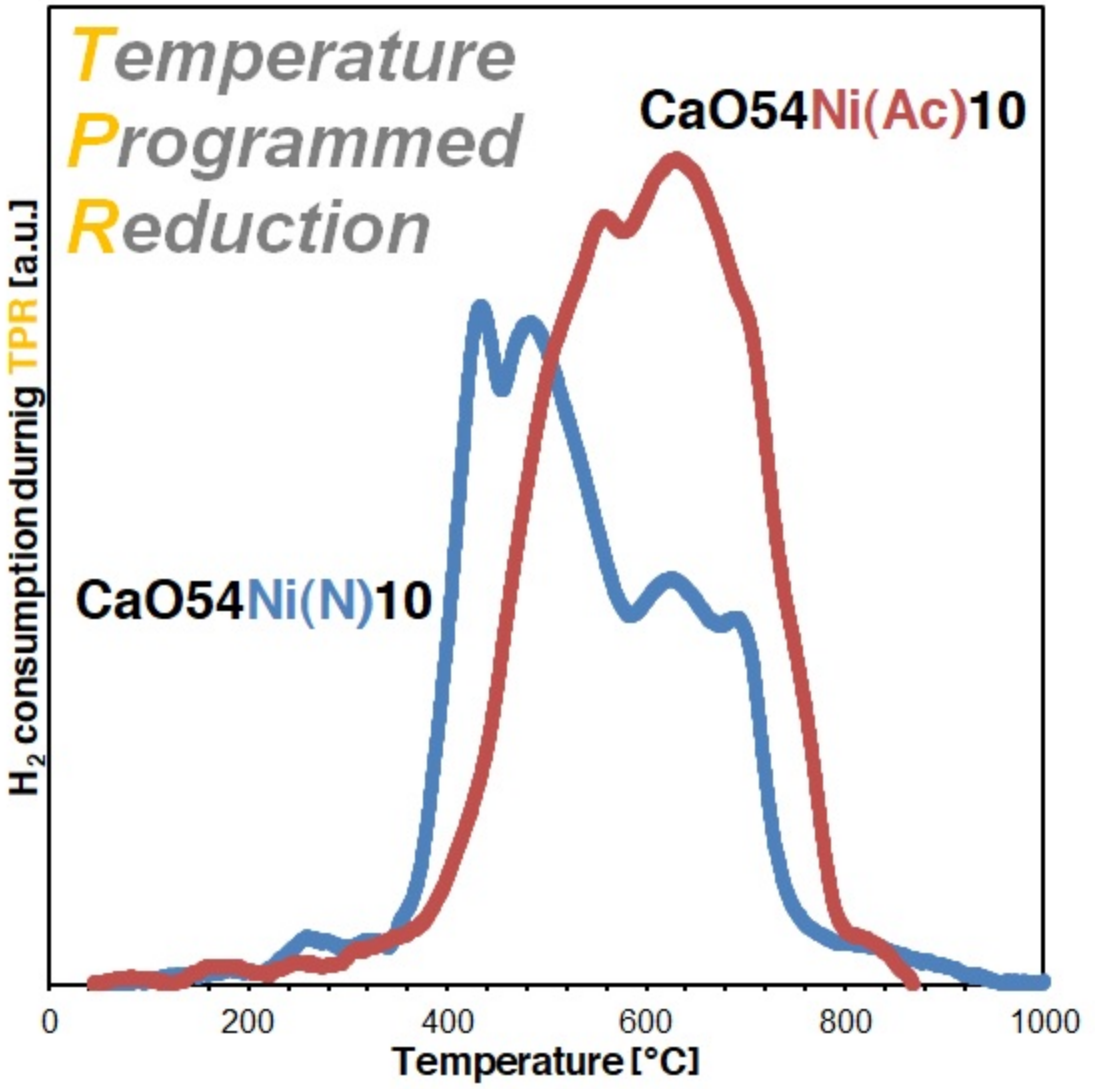
Temperature
Programmed
Reduction
CaO54Ni(Ac)10
CaO54Ni(N)10
H2 consumption durnig TPR [a.u.]
0
200
400
600
800
1000
Temperature [°C]

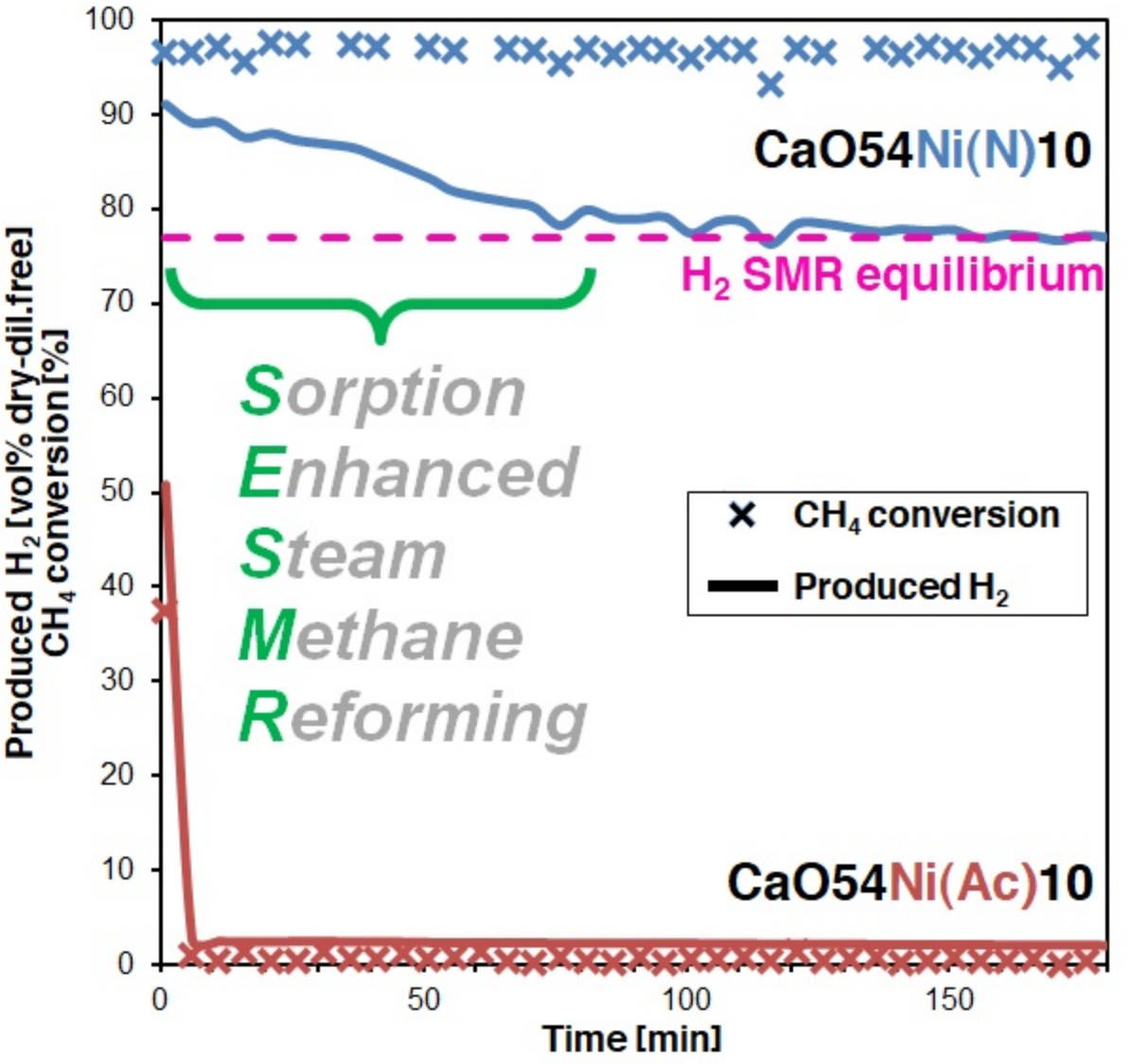
100
90
80
70
60
50
40
30
20
10
0
CaO54Ni(N)10
H2 SMR equilibrium
Sorption
Enhanced
Steam
Methane
Reforming
CH4 conversion
Produced H2
CaO54Ni(Ac)10
Produced H2 [vol% dry-dil.free]
CH4 conversion [%]
0
50
100
150
Time [min]